Tectono-geomorphological evolution of the Eastern Pyrenees: Insights from thermo-kinematic modeling

Gaétan Milesi, Pierre G Valla, Philippe Münch, Damien Huyghe

Accepted Manuscript published at Tectonophysics
(doi.org/10.1016/j.tecto.2023.230057)

Tectono-geomorphological evolution of the Eastern Pyrenees: insights from thermo-kinematic modeling

Gaétan Milesi[1,2,3], Pierre G. Valla[3], Philippe Münch[4], Damien Huyghe[5]

[1] GeoRessources, CNRS, Université de Lorraine, Labcom CREGU, 54506 Vandœuvre-lès-Nancy, France

[2] Chrono-Environnement, UMR 6249-CNRS, Université Bourgogne Franche-Comté, Besançon, France

[3] University of Grenoble Alpes, University of Savoie Mont Blanc, CNRS, IRD, IFSTTAR, ISTerre, 38000 Grenoble, France

[4] Géosciences Montpellier, Université de Montpellier, CNRS, Université des Antilles, Montpellier, France

[5] Mines ParisTech, PSL University, Centre de Géosciences, 35 rue St Honoré, 77305 Fontainebleau Cedex, France

Corresponding author: gaetan.milesi@univ-lorraine.fr

ABSTRACT

Constraining the tectono-geomorphological evolution of the Pyrenees is still a major challenge, especially in the Eastern Pyrenees where late Neogene exhumation history and topographic evolution appear contrasted and have been debated. In this study, we performed thermo-kinematic (Pecube) modeling using a relatively dense spatial compilation of previously-published low-temperature thermochronological data for the

Eastern Pyrenees, and quantified the late-Neogene exhumation history based on different topographic evolution models reconstructed from literature constraints. Our modeling outcomes suggest a major decrease in the regional exhumation rate between 37-35 Ma, associated to an early-end contractional tectonics for the Eastern Pyrenees. Two main periods of the Têt fault normal activity have been characterized, with the existence of pluri-kilometric (2-3 km) post- Oligocene-Miocene displacement along the western segment of the Têt fault. The different topographic evolution models show relatively similar results for the regional exhumation since ca. 35 Ma and for the most recent (mid to late-Miocene) tectonic event recorded along the Têt fault. Conversely, inversion results obtained for pre-35 Ma regional exhumation rates, and more importantly for the Oligocene-Miocene activity of the Têt fault appear contrasted between the investigated topographic scenarios. Overall, this study confirmed a mid to late Miocene significant extensional tectonic event for the Eastern Pyrenees, which may have had a non-negligible role in late-stage relief evolution for this part of the orogen. However, deciphering the long-term evolution of topographic relief through thermo-kinematic modeling appears still challenging for slowly-exhuming mountain ranges given the limited resolution of low-temperature thermochronological data to topographic changes.

KEYWORDS

Eastern Pyrenees, Low-temperature thermochronology, Tectonics, Thermo-kinematic models, Topographic evolution, Exhumation

1. INTRODUCTION

The Earth's surface evolution is controlled by the combination of tectonic, erosion and climate processes (e.g. Beaumont 1981; Willett, 1999; Dadson et al., 2003; Braun, 2010; Herman et al., 2013; Jamieson and Beaumont, 2013; Thieulot et al., 2014). The existence of feedbacks amongst these mechanisms (Whipple, 2009) constitutes one of the major difficulties to deconvolute the impact of each individual forcing on landscape dynamics (Braun, 2012). In the upper crust, isotherm shapes and wavelengths are especially controlled by the overlying topography and its evolution (Stüwe et al., 1994; Mancktelow and Grasemann, 1997; Braun, 2002; Foeken et al., 2007; Valla et al., 2010), therefore the upper-crust thermal evolution is influenced by rock exhumation and can be impacted by (i) major topographic changes or (ii) fault motion and associated isotherm advection (Batt and Braun, 1997; Ehlers and Chapman, 1999; Ehlers and Farley, 2003). Low-temperature (low-T) thermochronology coupled with 3D thermo-kinematic modeling provides a quantitative way to assess the crustal long-term thermal evolution and has the main advantage to investigate the respective contributions of the regional topographic evolution and/or the tectonic component(s) in rock exhumation (e.g. Farley, 2002; Ehlers and Farley, 2003; Glotzbach et al., 2011; Braun et al., 2012).

Thermo-kinematic 3D modeling based on low-T thermochronology data has been widely used in active mountain ranges to constrain the topographic evolution and fault-activity history, especially in mountain ranges with rapid changes in either topographic relief or tectonic forcing like for instance the Himalayas (e.g. Coutand et al., 2014; Zhang et al., 2015; Wang et al., 2016; Grujic et al.,2020; Pitard et al., 2021; Shen et al., 2022),

the Andean Cordillera (e.g. Schildgen et al., 2009, 2022; Avdievitch et al., 2018; Bermùdez et al., 2021; Gérard et al., 2021; Zapata et al., 2021) or the European Alps (e.g. Vernon et al., 2009; van der Beek et al., 2010; Valla et al., 2011, 2012; Beucher et al., 2012). However, only few 3D thermo-kinematic modeling studies have been devoted to the evolution of mountain ranges with limited or slow long-term topographic relief and tectonic evolution like the Pyrenees (i.e. Gibson et al., 2007; Fillon and van der Beek, 2012; Erdös et al., 2014; Curry et al., 2021; Capaldi et al., 2022). This approach is particularly challenging in mountain ranges formed by long tectonic histories with multiple phases since (1) overall exhumation rates can be relatively low between the different tectonic phases (<0.1 km/Ma; e.g. Braun and Robert, 2005), and (2) the topographic and tectonic settings and their long-term evolutions are complex. Therefore, it remains difficult to disentangle these two components in rock exhumation through low-T thermochronology in slowly-exhuming mountain range settings.

In the Pyrenees, regional 3D thermo-kinematic modeling has been focused on the central (Gibson et al., 2007; Erdos et al., 2014; Capaldi et al., 2022) and southern (Fillon and van der Beek, 2012) parts of the orogen. Recent study of Curry et al. (2021) has provided new quantitative constraints for the western and central part of the Axial Zone to evaluate thrust sheet-controlled exhumation as well as along-strike exhumation differences in the Pyrenees. Moreover, these previous studies have been particularly focused on the Paleogene Pyrenean contractional phase. The Eastern Pyrenees have a specific evolution, reflected by a complex tectonic history with an Eocene contractional phase (Laumonier, 2015; Ternois et al., 2019; Calvet et al., 2021; Ford et al., 2022)

followed by 2 significant post-orogenic periods: i) a transtensionnal phase associated with the opening of the West European Rift (Angrand and Mouthereau, 2021; Milesi et al., 2022), and ii) an Oligocene-Miocene extensional phase associated to the Gulf of Lion opening (Calvet et al., 2021; Jolivet et al.; 2020, 2021; Romagny et al., 2020; Séranne et al., 2021; Taillefer et al., 2021; Milesi et al., 2022). The Têt normal fault is the most prominent tectonic structure in the Eastern Pyrenees, and localizes high-relief massifs in such as the Mont-Louis (hanging wall), and the Canigou and Carança (footwall) massifs. The development of these high topographic reliefs has been related to normal faulting during the Oligocene-Miocene period (Maurel et al., 2008, Milesi et al., 2022). However, the topographic evolution of the area is still highly debated (e.g. Augusti et al., 2006; Gunnell et al., 2008, 2009; Suc and Fauquette, 2012; Calvet et al., 2014; Huyghe et al., 2018, 2020). The potential links between the topographic and tectonic evolutions of the Eastern Pyrenees are also not entirely clear due to their location between the contractional Pyrenean domain and the extensional area of the Gulf of Lion. Finally, the long-term topographic evolution of the Eastern Pyrenees (Huyghe et al., 2012, 2020) appears to differ significantly from the topographic evolution model proposed for the western and central parts of the Pyrenees (Curry et al., 2019; 2021).

In this study, we present the first 3D thermo-kinematic modeling outcomes for the Eastern Pyrenes, based on a large synthesis of previously-published (U-Th)/He on apatite (AHe) and zircon (ZHe), and apatite fission-track (AFT) data (Gunnell et al., 2009; Maurel et al., 2002, 2008; Milesi, et al., 2019, 2020a, 2020b, 2022). We also investigate 3 different models for the topographic evolution of the Eastern Pyrenees, with the objective

to integrate topographic evolution in 3D thermo-kinematic modeling and quantification of rock exhumation. By independently prescribing the long-term topographic evolution, we aim to provide constraints on the timing and rates of the Cenozoic to modern regional rock uplift as well as on the tectonic deformation along the Têt fault. Based on these results, we discuss the onset and timing of the contractional tectonic record in the Mont-Louis massif, and the late-Cenozoic extensional period(s) along the Têt fault in the Canigou and Carança massifs.

2. GEOLOGICAL SETTING

2.1 Topographic and tectonic evolution of the Pyrenees

In the Pyrenees, collision and orogen building occurred from the Late Cretaceous to the Middle Miocene (e.g. Roure et al., 1989; Muñoz, 1992; Vergés et al., 2002; Mouthereau et al., 2014; Ford et al., 2022), and formed a double-wedged mountain range. The Axial Zone (Fig. 1) is composed of a stack of crustal nappes formed during the main Eocene-early Oligocene orogenic build up and linked to the maximum of shortening and exhumation (Sinclair et al., 2005; Bosch et al., 2016a; Jolivet et al., 2007; Labaume et al., 2016; Mouthereau et al., 2014; Vacherat et al., 2016; Waldner et al., 2021). During the Lutetian (lower Eocene), the paleo-elevation of the Pyrenees has been estimated to around 2 ± 0.5 km (Huyghe et al., 2012), which is associated with the main phase of the Pyrenean orogen starting around 50 Ma (Fitzgerald et al., 1999; Sinclair et al., 2005; Vacherat et al., 2014, 2016; Ternois et al., 2019, 2021). Crustal flexural models (Curry et al., 2019) suggest topographic growth from 56 to 23 Ma and a sharp increase in topography at 38 Ma that is in contradiction with the more progressive topographic

136 growth deduced from stable isotope data (Huyghe et al., 2012). Flexural models showed a
137 minor decay of overall Pyrenean topography from 23 Ma to present-day. On the contrary,
138 the topographic model for the Eastern Pyrenees deduced from stable isotope analyses
139 (mammal teeth from the Cerdanya basin; Huyghe et al., 2020) suggests a slow relief
140 development since the Miocene (Fig. 2).
141
142 The exhumation history of the Pyrenees is marked by a southward propagation of
143 the orogenic-wedge deformation (Fitzgerald et al., 1999; Sinclair et al., 2005;
144 Mouthereau et al., 2014). The Pyrenean orogen has developed diachronously, from East
145 to West due to spatially-variable pre-orogenic crustal extension (e.g., Puigdefàbregas et
146 al., 1992; Whitchurch et al., 2011), some authors also proposed a role of major base-level
147 changes on the timing and rates of post-orogenic exhumation (Coney et al., 1996; Fillon
148 and van der Beek, 2012). Recent thermo-kinematic study from Curry et al. (2021) has
149 focused on the western and central part of the Pyrenees (Fig. 1) and, based on a large
150 compilation of low-T thermochronological data, their outcomes confirm a first-order
151 westward propagation of rock uplift and exhumation since the Eocene. This observed
152 propagation of tectonic deformation and exhumation may be explained by the inherited
153 crustal configuration rather than differential onset of shortening along strike (Teixell et
154 al., 2018; Muñoz, 2019). On the other hand, southward propagation of the deformation
155 (Fitzgerald et al., 1999; Sinclair et al., 2005; Metcalf et al., 2009) has been confirmed by
156 low-T thermochronology in the central part of the Pyrenees, while only geological
157 evidences support southward propagation of the deformation in the Western Pyrenees
158 (Teixell et al., 2016).

159

160 The post-orogenic tectonic evolution in the western and central Axial Zone has
161 not been well constrained. AHe ages from middle to late Miocene (15–6 Ma) are
162 interpreted in many ways, such as: (i) the result of a distinct tectonic event (Jolivet et al.,
163 2007; Bosch et al., 2016a; Fillon et al., 2021), (ii) the erosional response to major
164 drainage changes with the connection of the foreland Ebro Basin to the Mediterranean
165 Sea (Coney et al., 1996; Fitzgerald et al., 1999; Fillon and van der Beek, 2012), (iii)
166 large-scale erosion resulting from Pliocene climate changes, as proposed for the
167 European Alps (Cederbom et al., 2004), or (iv) a lithological control on post-orogenic
168 erosion with lower erosion rates for Variscan metamorphic lithologies in the eastern part
169 of the Axial Zone compared to unmetamorphosed lithologies in the western part (Bernard
170 et al., 2019). A recent thermochronological study in the Ebro basin (South Pyrenean
171 Zone) evidenced also a potential long-wavelength tectonic event at ~10 Ma, linked to the
172 cessation of slab retreat in the Western Mediterranean domain (Rat et al., 2022).

173

174 **2.2 Topographic and tectonic evolution of the Eastern Pyrenees**

175 The eastern part of the Axial Zone is characterized by the emplacement of south-
176 verging nappes rooted in the northern part (Laumonier et al., 2015; Sibuet et al., 2004;
177 Vergès et al., 1995; Teixell et al., 2016). Balanced cross-sections (Ternois et al., 2019)
178 suggest an Eocene thrusting of the Aspres-Mont-Louis massifs onto the Canigou massif
179 as already proposed by Maurel et al., (2008) based on low-T thermochronology. In
180 addition, the eastern part of the Pyrenees (east of ~1°E) underwent post-orogenic crustal
181 thinning (Chevrot et al., 2018; Diaz et al., 2018). This crustal-thinning phase has been

182 explained by regional extensional episodes associated to the (re-)activation of major
183 orogenic structures as normal faults in response to the Gulf of Lion opening from the end
184 of the Priabonian to the Quaternary (e.g. Calvet et al., 2021; Taillefer et al., 2021, Milesi
185 et al., 2022). In the study area (Fig. 1b), two main crustal tectonic structures are
186 identified: the Têt and Py faults. The most prominent tectonic structure, the Têt fault, is a
187 crustal-scale NE-SW fault with pluri-kilometric (~3 km) displacement associated to the
188 main opening stage (25-20 Ma) of the Gulf of Lion during the Oligocene-Miocene
189 (Maurel et al., 2008; Milesi et al., 2022). The Py fault delimits the Canigou and Carança
190 blocks in the footwall of the Têt fault (Fig. 1b), and recent thermochronological data
191 suggest a late Priabonian to early Rupelian (35-32 Ma) activity of this fault associated to
192 at least 2 km displacement (Milesi et al., 2022).
193
194 A major debate exists on the geomorphological evolution of the Eastern Pyrenees,
195 related to the formation timing and relative elevation of Oligocene-early Miocene high-
196 elevation low-relief surfaces (Bosch et al., 2016b; Monod et al., 2016; Calvet et al.,
197 2021). Some authors proposed the formation of these low-relief surfaces at low
198 elevations, followed by a major uplift event (~2 km) since the early Miocene (Gunnell et
199 al., 2008; 2009). Another model proposed the development of these low-relief surfaces at
200 high elevations due to the smoothing of the relief before the Late Miocene, associated to
201 a limited surface uplift of around 400 m since then (Babault et al. 2005; Bosch et al.,
202 2016b). Rock exhumation associated to late-Miocene normal faulting is considered to
203 have played a subordinate role, although significant exhumation events have been
204 proposed by (i) NW-SE fault activity (Taillefer et al., 2021) and (ii) thermal modeling in

the Carança massif, with predicted rock cooling between 12 to 9 Ma, interpreted as the normal motion of the western segment of the Têt fault (Milesi et al., 2022).

A paleo-elevation reconstruction for the whole Eastern Pyrenees, based on stable-isotope data coupled with regional geological constraints, has been proposed by Huyghe et al. (2020). This model suggests that the topographic uplift in the Eastern Pyrenees is a long-term process initiated in the Late Burdigalian (~20 Ma, Fig. 2) in response to the pre-breakup uplift in the Gulf of Lion. The Burdigalian period is considered as the end of the main rifting period for the western part of the Gulf of Lion. During this period, the topographic conditions in the Eastern Pyrenees were proposed to be close to sea level (Bache et al., 2010; Huyghe et al., 2020). The post-Burdigalian period in the Eastern Pyrenees is still debated, with a proposed uplift of ~1 km since the Tortonian to Messinian (i.e. since around 10 to 6 Ma) based on palynological constraints (Agusti et al., 2006; Suc and Fauquette, 2012). Stable-isotope data obtained from the analyses of small mammal teeth (Huyghe et al., 2020) complete these palynological data and suggest an uplift estimate of around 500 m since the Messinian (ca. 6 Ma). On the contrary, Tosal et al. (2021) recently proposed, from the study of leaf taxa, that the Cerdanya Basin was located at an elevation comprised between 1100 and 1500 m already during the Tortonian, although this estimate may reflect local conditions and should be confirmed by additional taxa analyses.

3. THERMO-KINEMATIC MODELING

3.1 Low-temperature thermochronology data in the Eastern Pyrenees

228 We focused our 3D thermo-kinematic modeling on the South Mérens, Carança and
229 Canigou blocks. The North Mérens block is not included due to the sparce low-T
230 thermochronological record in this area (Milesi et al., 2022). We compiled AHe, AFT,
231 ZHe ages and mean track lengths (MTL) from previously-published datasets (Gunnell et
232 al., 2009; Maurel et al., 2002, 2008; Milesi, et al., 2019, 2020a, 2020b, 2022). For our
233 study, we used only samples issued from crustal basement that record long-term rock
234 exhumation and were not affected by recent geothermal anomalies or hydrothermal
235 circulations (41 samples in total, Fig. 1b). In the Têt fault footwall, samples have been
236 selected in the first 5-km distance to the fault, since the cooling history of farther samples
237 may have been potentially impacted by other local faults. Details of the selected samples
238 and associated low-T thermochronological ages are available in the Supplementary Table
239 S1.
240
241 **3.2 Modeling approach**
242 Inverse modeling has been performed using the thermo-kinematic modeling code
243 Pecube v4.0, based on a finite-element method to solve the heat transport equation in 3D
244 (Braun, 2003; Braun et al., 2012), and coupled with the neighborhood algorithm (NA)
245 inversion method (Sambridge 1999a, 1999b). The detailed model setup is fully described
246 with all modeling parameters and our inversion approach in the Supplementary
247 Information.
248
249 We explored the 3 crustal blocks separately to constrain their respective rock
250 exhumation patterns: the South Mérens, Carança and Canigou blocks. No activity on the

Têt fault has been defined when modeling the South Mérens exhumation history (hanging wall of the Têt fault), only exhumation in response to regional uplift has been considered (Milesi et al., 2022). We modeled a two-stage regional exhumation model based on low-T thermochronological age-elevation relationships (Milesi et al., 2022) using AHe, ZHe AFT and MTL data (Supplementary Table S1). The model runs for 60 Myr, with a transition event between the two exhumation phases called "transition time" and ranging from 60 to 0 Ma. Each phase is associated to exhumation rates during the first (V1) and second (V2) phases, which range from 0 to 2 km/Ma and from 0 to 1 km/Ma, respectively. The output exhumation scenario obtained for the South Mérens block is thus considered as the regional exhumation scenario and used for subsequent modeling.

The Carança and Canigou blocks have been then investigated with prescribing an activity on the Têt fault. For the Canigou block, a single activity phase for the Têt fault has been tested following the work of Milesi et al. (2022). This approach is based on low-T thermochronological age-elevation relationships, which suggest a simple exhumation history for this area using AHe, ZHe AFT and MTL data. To further test this hypothesis, we have run an exhumation scenario with 2 activity phases for the Têt fault, however output results show poor inversion convergence for the tested parameters on the Têt fault activity (see Supplementary Figure S1). In the single-phase scenario, the model runs for 60 Myr, with a regional background exhumation fixed by best-fitting output results obtained in Section 4.1 (South Mérens block). The Têt fault activity is allowed between 35 and 5 Ma, with the onset time ranging from 35 to 25 Ma, and the ending time from 25 to 5 Ma. The fault slip rate ranges from 0 to 6 km/Ma.

For the Carança block, two potentially distinct activity phases for the Têt fault have been tested following the proposed thermal history of Milesi et al. (2022) using AHe, ZHe AFT and MTL data. The model runs for 60 Myr, with a regional background exhumation fixed by best-fitting output results obtained in Section 4.1 (South Mérens block). The first fault-activity phase is allowed between 35 and 15 Ma, with the onset time ranging from 35 to 25 Ma, and the ending time from 25 to 15 Ma. The fault slip rate during this first phase ranges from 0 to 6 km/Ma. The second fault-activity phase is allowed between 15 and 5 Ma, with the onset time ranging from 15 to 11 Ma, and the ending time from 11 to 5 Ma. The fault slip rate during the second phase ranges from 0 to 4 km/Ma.

Three main topographic evolution models (TEMs, Fig. 4) have been tested for the different crustal blocks: (1) a model without topographic change and a constant topography since 56 Ma which is similar to the present-day topography (Fig. 1b); (2) a Global Pyrenees model based on the topographic outcomes from Curry et al. (2019); and (3) an Eastern Pyrenees model (Fig. 2) based on the mean paleo-elevation curve proposed by Huyghe et al. (2020) and the maximum paleo-elevations defined by palynological constraints (Agusti et al., 2006; Suc and Fauquette, 2012). Due to the lack of continuous record for the maximum paleo-elevations, a conservative hypothesis has been established when no data is available. At 56 Ma, topographic parameters for the Eastern Pyrenees have been inferred from the literature, lower mean relief and topography have thus been implemented based on the lack of detrital material in adjacent basins, and the absence of alluvial cone/delta at that time (Calvet et al., 2021). All the parameters considered are

296 available in the Supplementary Table S2, and the mean paleo-elevation curves for the
297 three models, together with resulting topographies and associated topographic
298 amplification factor/offset, are illustrated in Figure 4.
299
300 **4. RESULTS**
301 **4.1 Hanging wall of the Têt fault: the South Mérens block**
302 Inversion results (Table 1) demonstrate that regardless of the considered TEM, the
303 1D probability density functions (PDFs) show no statistical convergence for the output
304 exhumation rates V1. However, we can note that all output values are above 0.2 km/Ma
305 and that a maximum of probability is reached for exhumation rates between 0.3 and 0.6
306 km/Ma for the Eastern Pyrenees TEM (Fig. 5). For the Global Pyrenees and No
307 topographic change TEMs, V1 is highly variable with a more pronounced probability
308 towards high exhumation rates (>0.5 km/Ma, Fig. 5).
309
310 The output transition time is well constrained and concordant for all three TEMs.
311 Inversion results for the transition time show a continuous probability distribution (40-30
312 Ma range), with a maximum probability between 37 and 35 Ma (Fig. 5).
313
314 The exhumation rate V2 is also well constrained for all three TEMs and varies
315 only slightly between them. The output PDFs for V2 are close to a Gaussian distribution,
316 with exhumation rates of 0.04 ± 0.03 km/Ma, 0.06 ± 0.01 km/Ma and 0.09 ± 0.03 km/Ma
317 for the No topographic change, the Global Pyrenees and Eastern Pyrenees TEMs,

318 respectively. Overall, the regional exhumation scenario for the different TEMs is very
319 well constrained between ~35 Ma and present day.
320
321 The best-fitting parameters obtained for each TEM have subsequently been used
322 in a forward Pecube model to predict low-T thermochronological ages and time-
323 temperature paths (Fig. 6). Low-T thermochronological ages modeled for the South
324 Mérens block are close to observed data, except for ZHe ages that are underestimated for
325 all considered TEMs (Fig. 6a). Modeled AHe ages with the Eastern Pyrenees TEM are
326 slightly younger for the top samples compared to the two other TEMs. Between 1600 and
327 2100 m, AHe ages are not well reproduced for all TEMs. However, it must be noted that
328 the observed AHe ages are older than AFT ages obtained at similar elevations. The
329 general trend of the AFT elevation profile is generally well reproduced with slightly older
330 modeled than observed ages. Predicted MTLs are relatively consistent between the used
331 TEMs, but overall overestimated the observed data except for mid-elevation samples
332 (~1600 m elevation, Fig. 6a).
333
334 Best-fitting predicted thermal histories (Fig. 6b) show similar overall trends, with
335 rapid cooling until ~35 Ma followed up by slow cooling until present day. Some
336 differences are observed between the considered TEMs: (i) before 35 Ma, the output
337 cooling rates are close to 17, 14 and 23 °C/Ma for the No topographic change, Eastern
338 Pyrenees and Global Pyrenees TEMs, respectively. Output cooling rates for this period
339 must be considered carefully when considering the large output PDFs and thus high
340 uncertainties obtained for V1 (Fig. 5d), with the better statistical estimate being given by

341 the Eastern Pyrenees TEM. (ii) Cooling rates after 35 Ma are more impacted by the
342 choice of the TEM. For the No topographic change TEM, the output cooling rate is
343 constant (~1 °C/Ma). The Global Pyrenees TEM yields a very low cooling rate between
344 35 and 23 Ma (~0.3 °C/Ma) which increased towards present day (1 °C/Ma). Finally, the
345 Eastern Pyrenees TEM yields a gradual decrease in cooling rate from 2.8 °C/Ma between
346 34 and 23 Ma to around 0.7 °C/Ma since 23 Ma.
347

348 **4.2 Eastern footwall of the Têt fault: the Canigou block**

349 Inversion results for the Têt fault activity (Table 1) slightly differ according to the
350 used TEMs. For the No topographic change and Global Pyrenees TEMs, the Têt fault
351 activity is limited in time with maximum probabilities from 26-25 to 24.5 Ma (Fig. 7a)
352 and from 28-26 to 24.5 Ma (Fig. 7b), respectively. Inversions based on the Eastern
353 Pyrenees TEM do not well constrain the fault-activity onset time but suggest a longer
354 activity period between >28 and 23.5 ± 1.5 Ma. These output differences are also marked
355 for the output fault slip rates (Fig. 7d). This parameter is not well constrained for the No
356 topographic change and Global Pyrenees TEMs, all inversions yielding high slip rates
357 above 1.0 and 1.5 km/Ma, respectively. In contrast, inversions with the Eastern Pyrenees
358 TEM show a maximum probability for output slip rate at 1 ± 0.5 km/Ma, significantly
359 lower than for other TEMs (Fig. 7d).
360

361 Predicted AHe ages are close for the No topographic change and Eastern Pyrenees
362 TEMs (Fig. 8a), and consistent with observed ages for elevation >1400 m. AHe ages
363 predicted with the Global Pyrenees TEM are younger than for the two other TEMs and

364 also compared to observed ages for elevation >1800 m. Observed AFT ages for top
365 samples (>2000 m) are well reproduced by numerical inversions with all the considered
366 TEMs (Fig. 8b). Only inversions with the Global Pyrenees TEM show predicted AFT
367 ages in agreement with observed ages for elevation <1600 m. Predicted MTLs differ
368 between the considered TEMs and samples: for most samples, the Global Pyrenees and
369 Eastern Pyrenees TEMs provided similar MTL predictions except for the low-elevation
370 sample for which predicted MTL differ for the Global Pyrenees TEM. The No
371 topographic change TEM predicted relatively short MTLs (<14 μm) and close to
372 observed data for most of samples, while the Global Pyrenees TEM produced shorter
373 MTL and close to observations for the low-elevation sample (Fig. 8a). The only ZHe age
374 in the Canigou block cannot be properly reproduced by numerical inversions whatever
375 the considered TEM, which all predict too young ZHe ages (Fig. 8a).
376
377 Best-fitting output thermal histories (Fig. 8b) show differences essentially due to
378 the contrasted timing and slip rate of the Têt fault activity (Fig. 7d). At around 25 Ma,
379 high cooling rates (~130 °C/Ma) are observed for the No topographic change TEM, while
380 slower cooling is predicted for the Global Pyrenees and Eastern Pyrenees TEMs (around
381 70 and 40°C/Ma, respectively). Posterior to this fault-activity phase, predicted cooling
382 rates are lower and consistent between all TEMs (2-4 °C/Ma, Fig. 7d).
383
384 **4.3 Western footwall of the Têt fault: the Carança block**
385 Inversion results for the first fault-activity phase (Table 1) differ according to the
386 used TEM (Fig. 9). For the No topographic change TEM (Fig. 9a), the first phase is

similar but slightly shorter compared to the Canigou block, i.e. from 26-25 to 25-24 Ma, and associated with a high slip rate (maximum of probability at 5.5-6 km/Ma). The Global Pyrenees TEM (Fig. 9b) suggests a longer fault activity between 28 ± 2 and around 25-24 Ma. The output slip rate is not well constrained. For inversions based on these 2 TEMs (No topographic change and Global Pyrenees), the first phase of the Carança block appears similar to the predicted fault activity of the Canigou block. Inversions based on the Eastern Pyrenees TEM suggest a longer fault activity, with a maximum probability for the onset time at 32 ± 1 Ma and ending time at around 15 Ma. For this TEM, the end of first fault-activity phase is thus suggested later than for the Canigou block. Inversions based on the Eastern Pyrenees TEM yield a well-constrained slip rate of <1 km/Ma that is lower than for the other TEMs (Fig. 9d) but consistent with output slip rate for the Canigou block (Fig. 7d).

The inversion outcomes for the second fault-activity phase (Table 1 and Fig. 10) are similar whatever the considered TEM. Inversion results show a maximum probability for the fault-activity duration between around 15 and 11 Ma. The PDFs for the slip rate are close to Gaussian distributions, with a maximum probability in the range of 0.7-0.8 km/Ma (Fig. 10d).

Predicted AHe ages are close for the 3 considered TEMs but they overall underestimate the observed AHe ages. Output AHe ages are rather consistent with observed low-elevation ages (1050-1250m, Fig. 11a). Predicted AFT ages are consistent or very close to the observed ages for all considered TEMs. Predicted ZHe ages are

410 different according to the used TEMs, being increasingly younger for inversions based on
411 the Global Pyrenees, Eastern Pyrenees and No topographic change TEMs, respectively.
412 Modeled ZHe ages with the Global Pyrenees TEM are close to observed ages for the base
413 of the elevation profile (900-1000 m) whereas predictions with the No topographic
414 change TEM are more coherent with observed ages (1200-1400 m). Predicted MTLs are
415 well reproducing observed data for the different TEMs (Fig. 11a). All TEM models fail to
416 explain observed ZHe ages (>1600 m), and predict rather young ZHe ages compared to
417 observations (Fig. 11a).
418
419 Best-fitting output thermal histories (Fig. 11b) show differences between TEMs
420 that are essentially due to the contrasted duration and intensity of the first fault-activity
421 phase (Fig. 9d). The main differences are similar to those obtained for the Canigou
422 inversions (Section 4.2). For the first phase, high cooling rates are observed for the No
423 topographic change (~140 °C/Ma) and Global Pyrenees TEMs (~70 °C/Ma), while
424 slower cooling is predicted for the Eastern Pyrenees TEM (~10 °C/Ma). This first cooling
425 phase is followed by a decrease in cooling rate regardless of the TEM (<5 °C/Ma).
426 Output thermal histories show a similar pattern between 15 Ma and present day between
427 the three TEMs: output cooling at ~20 °C/Ma associated to the second fault-activity
428 phase between 15 and 11 Ma, followed by slow cooling (1-2° C/Ma, Fig. 11b).
429
430 **5. DISCUSSION**
431 **5.1 Pyrenean contractional stage**

Our inversion results allow reconstructing a two-stage regional exhumation history for the South Mérens block (hanging wall of the Têt faut, Fig. 1), with a well-constrained transition time between 37 and 35 Ma regardless of the considered TEM (Fig. 5). Exhumation rates V1 are not well constrained, with a probability peak between 0.3 and 0.6 km/Ma for the Eastern Pyrenees TEM and >0.5 km/Ma for the global Pyrenees and No topographic change TEMs. Exhumation rates V2 appear significantly lower and are well constrained (close to Gaussian distributions) below 0.1 km/Ma for all the TEMs. These results overall agree with thermal histories obtained with QTQt modeling, showing rapid cooling between 40 and 35 Ma, followed by slow cooling since 35 Ma (Milesi et al., 2022, Fig. 12). The regional exhumation scenario for the different TEMs is also very well constrained between ~35 Ma and present day, which is the main period of interest for this study. More complex exhumation scenarios (e.g. considering a three-phase exhumation history) have also been tested, without significant improvement regarding low-T thermochronological age predictions (Milesi, 2020).

Best-fitting inversion models showed similar thermal-history predictions for the 3 TEMs, only slightly influenced by the topographic evolution after 35 Ma (Fig. 6). Cooling rates associated to the first exhumation phase are between 15 and 20°C/Ma, consistent at first order with QTQt outcomes. However, QTQt results (Milesi et al., 2022) suggested an apparent two-stage cooling history before 35 Ma: a first phase between 50 and 38 Ma (>5°C/Ma) followed by a second phase between 38 and35 Ma (~30°C/Ma). This two-stage history is not constrained in Pecube-derived thermal histories (Fig. 12), which can be explained by both the relative simplicity of our implemented Pecube exhumation scenarios (i.e. only two exhumation phases considered) but also by the lack

455 of low-T thermochronological data for the 50-38 Ma period (Fig. 6 and Table S1).
456 Indeed, most of ZHe and AFT data from high-elevation samples are not well reproduced
457 whatever the considered TEMs (Fig. 6).
458
459 Predicted cooling rates associated to the second exhumation phase showed slight
460 differences between the considered TEMs, but are overall quite low (up to 1°C/Ma,
461 except for the Eastern Pyrenees TEM with 2.8 °C/Ma between 34 and 23 Ma, Fig. 6).
462 Observed AHe and AFT data are well reproduced by our best-fitting Pecube models,
463 except for samples characterized by ages inversion (i.e. AHe ages are older than AFT
464 ages). Such an ages inversion cannot be reproduced by Pecube due to the relatively
465 simple AHe diffusion model used in this code (Braun et al., 2012), since for example it
466 does not consider apatite chemistry nor size effects on He diffusion (see Section 3.2; e.g.
467 Gautheron et al., 2009).
468
469 Predicted regional exhumation rates prior to ca. 35 Ma are all above 0.2 km/Ma,
470 with PDF peaks for rates >0.3 km/Ma from our inversion results (Figs. 5 and 12) that can
471 be related to the activity of major regional thrusts located further South of the Mérens
472 block (Fig. 1a), like the Cadi-Canigou thrust (Ternois et al., 2019). Regional thrusting in
473 the Eastern Pyrenees has been linked to the contractional phase of the orogen, associated
474 to the convergence between the Iberian and European plates during the Eocene
475 (Fitzgerald et al., 1999; Whitchurch et al., 2011; Rushlow et al., 2013; Mouthereau et al.,
476 2014; Bosch et al., 2016a; Labaume et al., 2016; Cruset el al., 2020). The end of this
477 contractional phase is well constrained in our inversion results between 37 and 35 Ma,

478 followed by a major decrease of exhumation rates (<0.1 km/Ma) for the eastern part of
479 the Axial Zone (Fig. 1), which contrasts with faster exhumation rates at 1.0 ± 0.1 km/Ma
480 proposed further West between 40 and 30 Ma (Curry et al., 2021). These exhumation
481 differences can first be explained by our model set-up, for which the transition time is an
482 inversion parameter and not constrained by an a priori prescribed time window (see
483 Section 4.1) as in Curry et al. (2021). In addition, we propose that this temporal
484 difference may reflect a first-order westward propagation of rock uplift and exhumation
485 starting in the eastern part of the Pyrenees (Whitchurch et al., 2011; Fillon et al., 2016;
486 Curry et al., 2021). The observed early end of the contractional event corresponds also to
487 the proposed period for the onset of extensional tectonics in the Eastern Pyrenees,
488 associated with the large-scale West European Rifting (Ziegler, 1992; Romagny et al.,
489 2020; Angrand and Mouthereau, 2021; Jolivet et al., 2021; Mouthereau et al., 2021;
490 Séranne et al., 2021; Milesi et al., 2022).
491
492
493 **5.2 Têt fault activity**
494 **5.2.1 The Canigou block**
495 Inversion results for the Têt fault activity differ according to the used TEM, but
496 overall our model outcomes reveal that the fault-activity duration is not well constrained
497 (Fig. 7). For the No topographic change and Global Pyrenees TEMs, the Têt fault activity
498 appears shorter in time (from 26-25 to 24.5 Ma and 28-26 to 24.5 Ma, respectively)
499 compared to the Eastern Pyrenees TEM (between >28 Ma and 23.5 ±1.5 Ma).
500 Consistently, predicted fault slip rates are also not well constrained for the different

TEMs (Figure 7e) but they appear relatively high and unconstrained for the No topographic change (1.0-6.0 km/Ma) and Global Pyrenees (1.5-6.0 km/Ma) TEMs, while they seem slightly lower and more constrained for the Eastern Pyrenees TEM (1 ± 0.5 km/Ma). Output slip rates can be translated into vertical rock uplift/exhumation rates using the implemented fault dip in Pecube models, with the following estimates: >0.85 km/Ma, >1.3 km/Ma and 0.85 ± 0.40 km/Ma for the No topographic change, Global Pyrenees and Eastern Pyrenees TEMs, respectively. All these estimates are well higher than output exhumation rates of 0.33 to 0.56 km/Ma derived from age-elevation relationships for the same period (Milesi et al., 2022). However, our estimated exhumation rates associated to the Têt fault activity are in the same order of magnitude than exhumation rates obtained by thermochronological studies along other normal faults worldwide (e.g. Fletcher et al., 2000; Ehlers et al., 2001). These differences of exhumation rates can be explained by the simple diffusion models used in Pecube code and modeling assumptions (see Section 3.2).

Best-fitting inversion models show a good agreement between model predictions and observed low-T thermochronological ages (Fig. 8), with noticeable differences between the No topographic change/Eastern Pyrenees TEMs and the Global Pyrenees TEM. The main differences are illustrated by AHe and low-elevation AFT ages predicted for the Global Pyrenees TEM, which are younger than for the two other TEMs. These differences are also visible in output thermal histories, with a more pronounced cooling event (~120 °C/Ma) for the Global Pyrenees TEM than for the two other TEMs (~90 °C/Ma). In contrast with the QTQt output Oligocene-Miocene cooling rates (~30 °C/Ma,

Fig. 12), Pecube thermal histories reveal faster cooling during that period. It is particularly visible for Global Pyrenees and Eastern Pyrenees TEMs (Fig. 8b), with prescribed Oligocene-Miocene cooling from 350°C to 120°C and 260°C to 30°C, respectively. These important differences can be due to the potential combination of 2 independent cooling phases in our Pecube approach: a Priabonian cooling phase, followed by a second Oligocene-Miocene phase, which are predicted for QTQt modeling (Fig. 12, Milesi et al., 2022). Furthermore, these output thermal histories are reflecting the complexity to properly model the observed ZHe age for the Canigou block (Fig. 8a) and the MTL data from top-profile samples of the Canigou block (Fig. 8b). Performed inversion models with 2 fault-activity periods tend to refine fault slip rates during the Oligocene-Miocene phase rather than highlighting a Priabonian tectonic event, most certainly due to the lack of data for this period (Supplementary Table S1 and Figure S1). It is important to note that with the Eastern Pyrenees TEM, the output fault activity is starting earlier (~28 Ma) which is closer to the observed ZHe age. Additional ZHe and ZFT data in the Canigou area would allow to better constrain this early tectonic phase. Considering our inversion results and the relatively good AHe/AFT model predictions, no post Oligocene-Miocene activity of the Têt fault is required to explain low-T thermochronological data in the Canigou block.

5.2.2 The Carança block

Inversion results for the first fault-activity phase differ according to the considered TEM (Fig. 12). For the No topographic change TEM, this first phase appears limited in time (from 26-25 Ma to 25-24 Ma). The Global Pyrenees TEM suggests a

547 slightly earlier onset of fault activity (28 ± 2 Ma) but close ending time (25-24 Ma),
548 similarly to the Canigou block (Section 5.2.1). Inversions based on the Eastern Pyrenees
549 TEM suggest a longer fault activity, between around 32 Ma and 15 Ma. Estimated faut
550 slip rates are high (5.5-6 km/Ma) for the No topographic change TEM, these are much
551 lower for the Eastern Pyrenees TEM (<1 km/Ma) and not well constrained for the Global
552 Pyrenees model (Fig. 10d). These differences in quantitatively constraining fault slip
553 rates can be explained by the major differences in the low-T thermochronological dataset
554 for the Carança block compared to the Canigou block, with a complete ZHe age-elevation
555 profile and low-elevation AHe ages that record exhumation for the mid to late Miocene
556 period (Fig. 11a). Output Oligocene-Miocene cooling rates (Fig. 11) are relatively high
557 (>100 °C/Ma) for the No topographic change and Global Pyrenees TEMs, similar to the
558 Canigou block (Fig. 9), while slower cooling is predicted for the Eastern Pyrenees TEM
559 (~10 °C/Ma). However, the output cooling rate for the Global Pyrenees TEM has to be
560 considered cautiously and may not be representative due to the largely unconstrained
561 fault slip rate with this TEM (Fig. 10d). Finally, our results suggest the existence of
562 diachronism and magnitude differences for the Têt fault activity along its western
563 segment (i.e. Canigou vs. Carança block), confirming previous observations with QTQt
564 models (Fig. 12; Milesi et al., 2022).
565
566 Predictions for the second fault-activity phase are relatively similar whatever the
567 considered TEM. Inversion results for the fault duration show a maximum probability
568 between around 15 and 11 Ma, with an associated fault slip rate of 0.7-0.8 km/Ma (Fig.
569 10). These results indicate the existence of a major post Oligocene-Miocene activity of

570 the Têt fault along the Carança block, with associated rock exhumation (estimated using
571 slip-rate predictions and Têt-fault dip) above 0.6 km/Ma that is 5-10 times higher than the
572 regional exhumation rate recorded in the South Mérens block (see Section 5.1) over the
573 same period. Independently of the considered TEM, the low-T thermochronological
574 dataset for the Carança block cannot be only explained by large-scale change(s) in
575 topographic relief (Gunnell et al., 2008; Huyghe et al., 2020; Calvet et al., 2021). Output
576 cooling at about 20 °C/Ma is associated with this late-stage tectonic exhumation phase
577 between 15 and 11 Ma, and is consistent to first order with the previously recognized
578 cooling phase, but of lower magnitude (around 10 °C/Ma) and duration (between 11 and
579 9 Ma), in QTQt thermal models (Milesi et al., 2022). Observed differences between the
580 two modeling approaches (Pecube vs. QTQt) can be explained by (i) the relatively simple
581 He diffusion model used in Pecube (see Section 3.2), and (ii) the lack of topographic
582 evolution in QTQt modeling approach. Overall, our results indicate a major tectonic stage
583 during the middle to late Miocene, with kilometric-scale (2-3 km) displacement inferred
584 on the Têt fault along the Carança block only, which cannot be reproduced for the
585 Canigou block (Supplementary Figure S1). This fault-displacement estimate is much
586 higher than the previously-proposed 150-500 m for this period and applied
587 homogeneously along the Têt fault (Pous et al., 1986; Réhault et al., 1987; Roca &
588 Desegaulx, 1992; Calvet, 1999; Carozza & Baize, 2004; Delcaillau et al., 2004; Agustì et
589 al., 2006). Our results are also consistent with a westward propagation of the deformation
590 along the Têt fault with a proposed more recent activity along the Carança block
591 compared to the Canigou block (Carozza & Delcaillau, 1999; Carozza & Baize, 2004;
592 Milesi et al., 2022), marked by the more recent activity along the Carança block

593 compared to the Canigou block, and the latest activity of the Têt fault further West, along
594 the Cerdanya Basin, during late Miocene times (Pous et al., 1986; Agustì et al., 2006).
595
596 The main differences between observed and predicted low-T thermochronological
597 ages (Fig. 11a) are essentially marked for high-elevation ZHe and AHe ages. ZHe age
598 differences may be linked to lateral variations in timing and exhumation rates associated
599 to the contractional deformation phase in the Eastern Pyrenees as it has been observed at
600 the scale of the whole Pyrenees (Curry et al., 2021). In addition, AHe ages located below
601 1400 m elevation show an important dispersion between 15 and 20 Ma. This observed
602 dispersion can be explained by (i) differences in apatite U-Th content and grain size
603 (Milesi et al., 2022), and/or (ii) additional activity of secondary NW-SE fault(s) between
604 20 and 15 Ma (Fig. 1b). These NW-SE faults are particularly well expressed in the
605 western part of the study area (Taillefer et al., 2021) and can create an important
606 segmentation of the Carança block, therefore resulting in slightly different cooling
607 histories within the different sub-blocks. The potential activity of such NW-SE faults
608 could also explain the local elevation increase of the Cerdanya basin documented by
609 Tosal et al. (2021) during late Miocene-Pliocene times.
610
611 **5.3 Tectono-geomorphological evolution of the Eastern Pyrenees**
612 The original approach of our study was to assess regional exhumation and
613 tectonic histories from 3D Pecube inversions using contrasted TEMs over the last around
614 60 Myr (Fig. 4). Figure 13 summarizes the three tested topographic evolution scenarios
615 along with the output key periods in exhumation/tectonic activity:

- (i) Prior to 37 Ma for the South Mérens block, inferred exhumation rates are significantly higher for the Global Pyrenees or No topographic change TEMs (>0.5 km/Ma) compared to the Eastern Pyrenees TEM (0.3-0.6 km/Ma);

- (ii) since around 37-35 Ma, i.e. the end of the contractional phase, until present day, inferred regional exhumation rates are very close (0.04-0.09 km/Ma, Fig. 12), whatever the considered TEM;

- (iii) from 33 to 15 Ma, corresponding to the main Têt-fault activity period along the Canigou and Carança blocks (phase 1), the Global Pyrenees and No topographic change TEMs predict a shorter phase with much higher fault-slip rates compared to inversions with the Eastern Pyrenees TEM (Fig. 12). As these differences are observed for both the Canigou and Carança blocks, our results confirm that the topographic relief evolution scenarios have had a significant impact on the thermochronology cooling ages predicted by the model;

- (iv) between 15 and 11 Ma, a second fault-activity phase but only along the Carança block is inferred from our Pecube inversions whatever the considered TEM. Output fault-slip rates are also very consistent for the different TEMs, between 0.7 and 0.8 km/Ma (Fig. 10d).

Overall, these results show that it remains difficult to use low-T thermochronological data from the Eastern Pyrenees to quantitatively assess the long-term topographic evolution of the area, even if the proposed topographic evolution models since ca. 60 Ma are very contrasted (Fig. 13). We suggest the possible following reason for this limitation: topographic relief changes for the Eastern Pyrenees, even if

639 they appear important in amplitude, are spread out over tens of millions of years, limiting
640 their impact on the crustal thermal structure and rock exhumation compared to the
641 regional rock uplift and local fault activity (Valla et al., 2010; 2011).
642
643 Despite the lack of quantitative information on the robustness of the different
644 TEMs from low-T thermochronology, this approach allowed us to highlight and quantify
645 the main extensional tectonic events that have affected the Eastern Pyrenees. Our results
646 confirm a major Oligocene-Miocene displacement (pluri-kilometric) along the Têt fault,
647 confirming previously-proposed interpretations for the Canigou massif (Maurel et al.,
648 2008; Milesi et al., 2022). This major tectonic phase may be related to the opening of the
649 Gulf of Lion (e.g. Séranne, 1999; Mauffret et al., 2001; Maillard et al., 2020; Romagny et
650 al., 2020; Jolivet et al., 2021). Our new results moreover highlight some differences in
651 fault timing and slip rates for this extensional phase between the Carança and Canigou
652 blocks, even though these results must be considered carefully, in particular for the
653 Canigou block, due to the potential contribution of an earlier fault-activity phase during
654 the Priabonian. One major outcome of this study is the characterization of a second, post
655 Oligocene-Miocene, extensional tectonic event between 15 and 11 Ma, with kilometric
656 displacement associated along the Têt fault but restricted to its western segment (i.e. the
657 Carança block). Even if this episode is less important in magnitude than the Oligocene-
658 Miocene one, this has been triggering important displacement along the western part of
659 the Têt fault, and can have significantly contributed to the regional relief changes
660 recorded in the Eastern Pyrenees (Gunnell et al., 2008; Huyghe et al., 2020; Calvet et al.,
661 2021). This tectonic event may have been recorded at the scale of the whole Pyrenees, as

662 recent thermochronological evidence in the Ebro basin (South Pyrenean Zone) have
663 highlighted a long-wavelength tectonic event at ~10 Ma (Rat et al., 2022) similar to what
664 was also proposed for the western part of the Pyrenees (Fillon et al., 2021). Our study
665 provides further evidence for large-scale lithospheric and sub-lithospheric processes,
666 particularly well expressed in the Eastern Pyrenees, that coincide with the cessation of
667 slab retreat in the West Mediterranean Sea (Jolivet et al., 2021).

668

669 **CONCLUSIONS**

670 3D Pecube thermo-kinematic inversions, using different topographic evolution
671 models for the Eastern Pyrenees, reveal a major decrease in regional exhumation rates
672 between 37-35 Ma. This change is associated to an early end of the contractional tectonic
673 period in the Eastern part of the orogen, while deformation and rock exhumation
674 propagated to the West. The detailed investigation of the Têt fault activity along the
675 Canigou and Carança blocks has been favored by the dense existing low-T
676 thermochronological datasets. Our inversion results highlight two main period of normal-
677 fault activity with (i) a major Oligocene-Miocene phase recorded in the Canigou and
678 Carança blocks, (ii) a secondary mid- to late-Miocene phase with, however, kilometric
679 displacement (2-3 km) restricted along the western segment of the Têt fault (Carança
680 block), and (iii) no latest Miocene or Pliocene major phase that could have been recorded
681 by low-T thermochronometers. These outcomes confirmed the presence of significant
682 extensional tectonics in the Eastern Pyrenees that may have had a non-negligible role in
683 the late-stage construction of the topographic relief. Finally, our approach and results
684 highlight the benefits of integrating long-term topographic evolution models at a regional

685 scale to further constrain the exhumation and tectonic histories from low-T
686 thermochronological data and inverse 3D thermo-kinematic modeling.
687
688 **ACKNOWLEDGMENTS**
689 This research received funding from the program TelluS of the Institut National
690 des Sciences de l'Univers, CNRS. Thanks for technical support with Pecube code go to J.
691 Braun and B. Gérard. G.M acknowledges D. Whipp and I. Kukkonen for the organization
692 of the short course on low temperature thermochronology 2017 and first steps with
693 Pecube modeling at the University of Helsinki. P.G.V. acknowledges funding from the
694 French ANR-PIA program (ANR-18-MPGA-0006). We thank M.E. Curry and F.
695 Mouthereau for their positive and constructive reviews that clearly helped improving our
696 manuscript.
697
698 ## Supplementary Information
699 Supplementary Information to this article can be found online at ...
700

FIGURES AND CAPTIONS

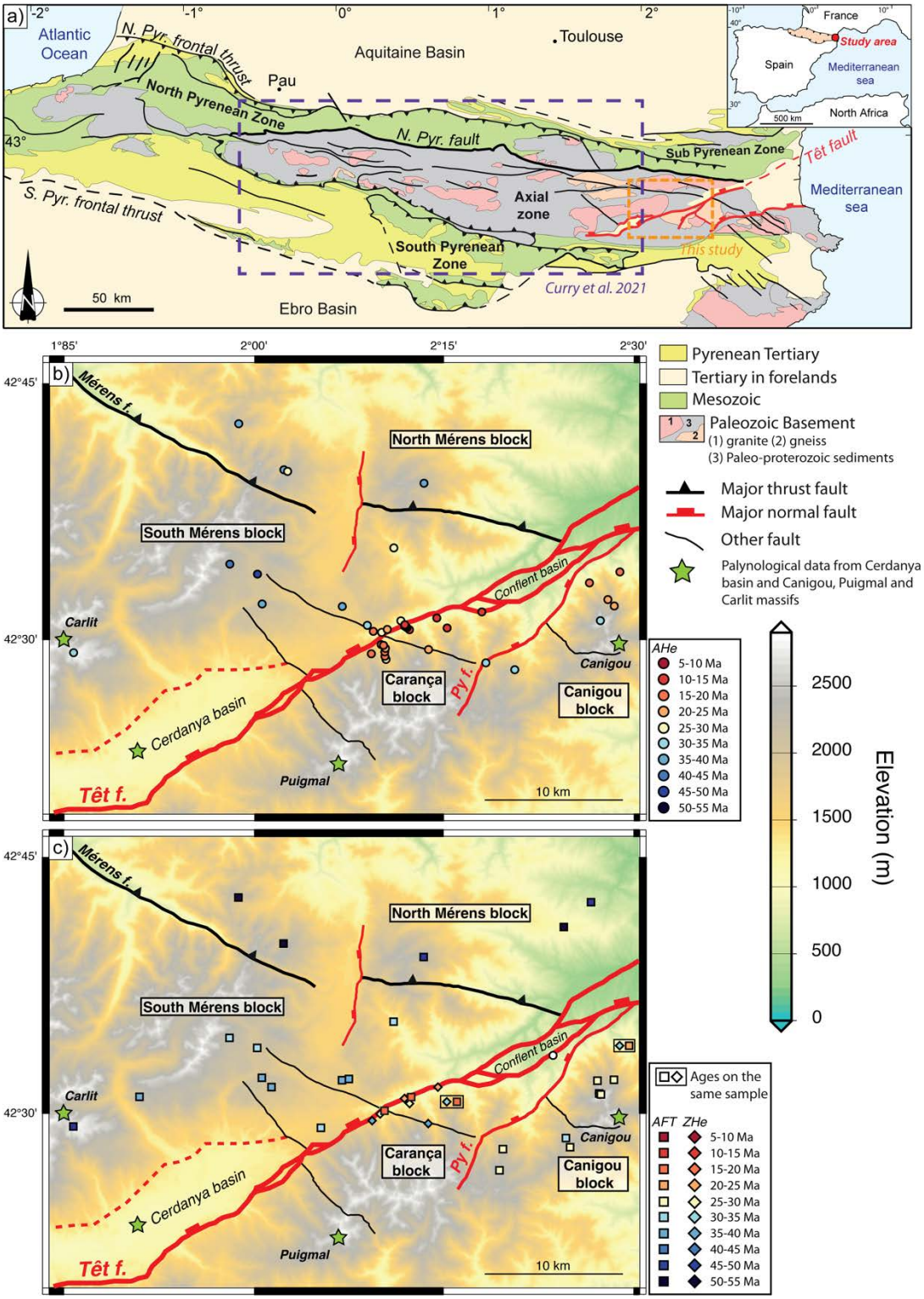

Figure 1. a) Geological map showing the main structural domains of the Pyrenees (modified after Taillefer et al., 2017). The main Neogene normal faults of the Eastern

Pyrenees are reported in red. The area delimited for 3D thermo-kinematic modeling from Curry et al. (2021) is outlined with a purple-dashed box, and our study area with an orange-dashed box. b) Location of AHe ages and c) AFT and ZHe ages (literature data, see text for details) projected on SRTM1s DEM under GMT (Wessel et al., 2019). The different crustal blocks (South and North Mérens in the Mont Louis massif, Carança and Canigou) are delimited by regional major faults (bold italics, modified after Milesi et al., 2022), while secondary faults and main basins (Cerdanya, Conflent) are also indicated. Location of palynological data discussed in the main text are indicated by green stars in panels b-c.

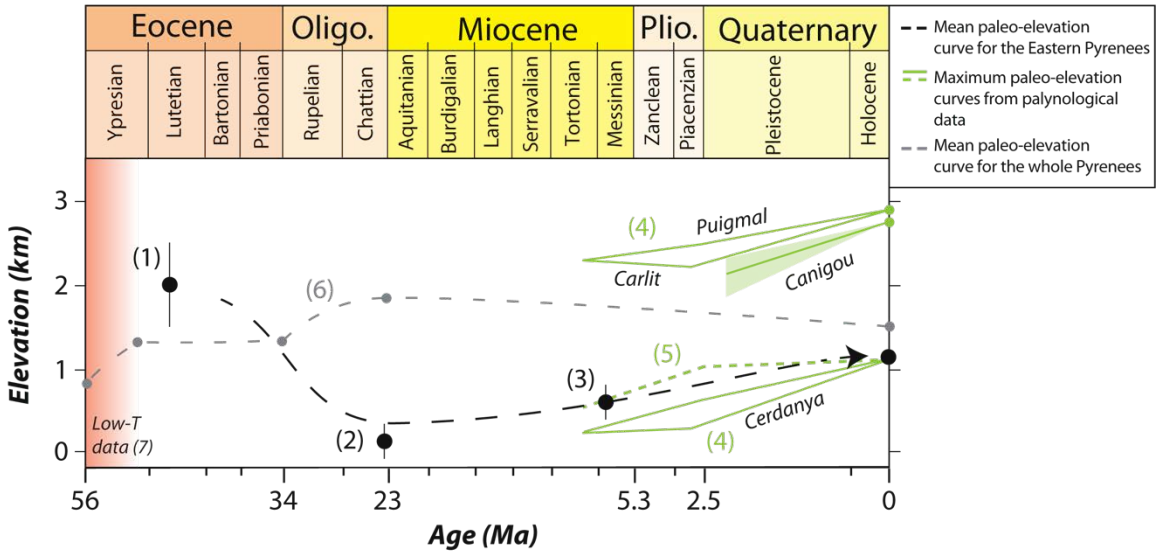

714

715 Figure 2. Topographic relief evolution for the Eastern Pyrenees since Ypresian times
716 (modified after Huyghe et al., 2020). Mean paleo-elevation curve for the Eastern
717 Pyrenees is based on studies from (1) Huyghe et al. (2012); (2) Bache et al. (2010); (3)
718 Huyghe et al. (2020). Maximum paleo-elevation curves are issued from palynological
719 data from (4) Suc and Fauquette (2012) and (5) Agusti et al. (2006), Mean paleo-
720 elevation curve for the whole Pyrenees is issued from (6) flexural model outputs from
721 Curry et al. (2019), and (7) low-T thermochronological studies from Fitzgerald et al.
722 (1999); Sinclair et al. (2005); Vacherat et al. (2014, 2016) and Ternois et al. (2019,
723 2021).

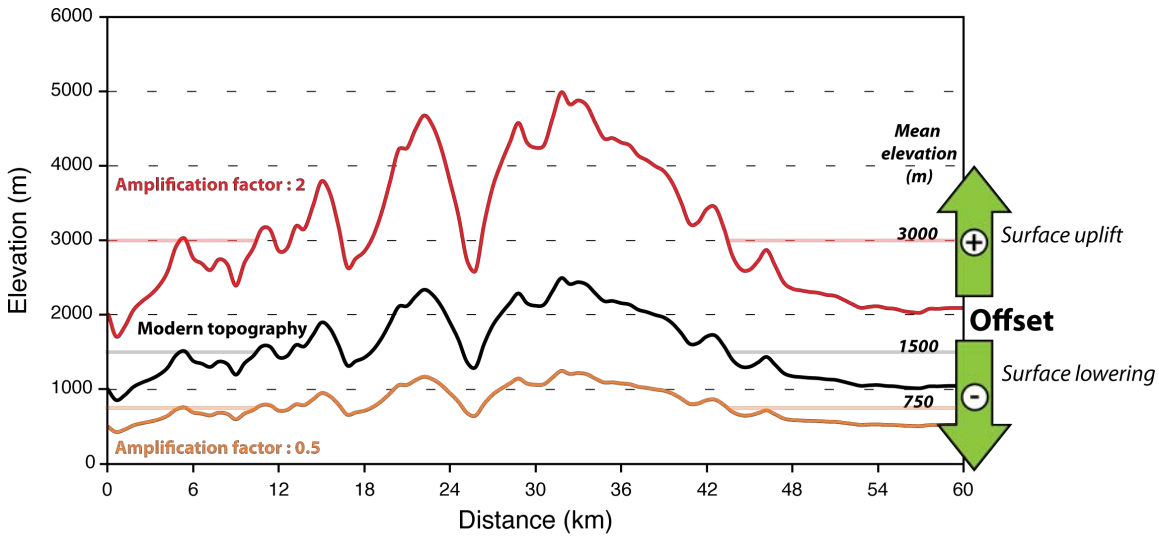

Figure 3. Topographic profile of the Canigou massif to schematically illustrate the impact of the amplification factor and offset parameters used to describe topographic changes in Pecube modeling. Different scenarios are considered with (1) an amplification factor of 2 and offset of 1500 m (red line) and (2) an amplification factor of 0.5 and offset of -750 m (orange line). The modern topography (amplification factor 1 and offset 0 m) is shown by the black line.

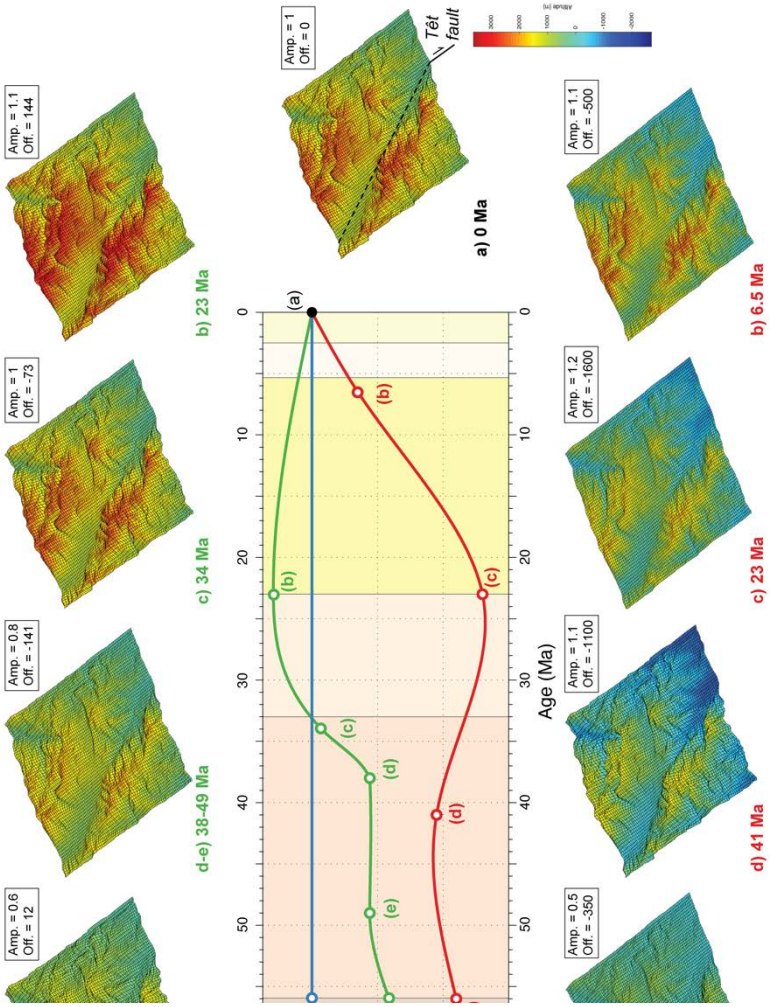

Figure 4. Three topographic evolution models (TEMs) used for Pecube thermo-kinematic modeling. In blue is represented the TEM for the No topographic change. In green is shown the TEM for the Global Pyrenees issued after Curry et al. (2019). Finally, in red appears the TEM for the Eastern Pyrenees (after Huyghe et al., 2020; see Section 3.3 for further details). The resulting DEM for each evolution step is presented (upper: Global Pyrenees; lower: Eastern Pyrenees) with associated values of amplification factor (Amp.) and offset (Off.) in meters (see Section 3.2 and Supplementary Table S2 for full details). The surface trace of the normal Têt fault implemented in Pecube models is represented in the modern DEM (dashed black line).

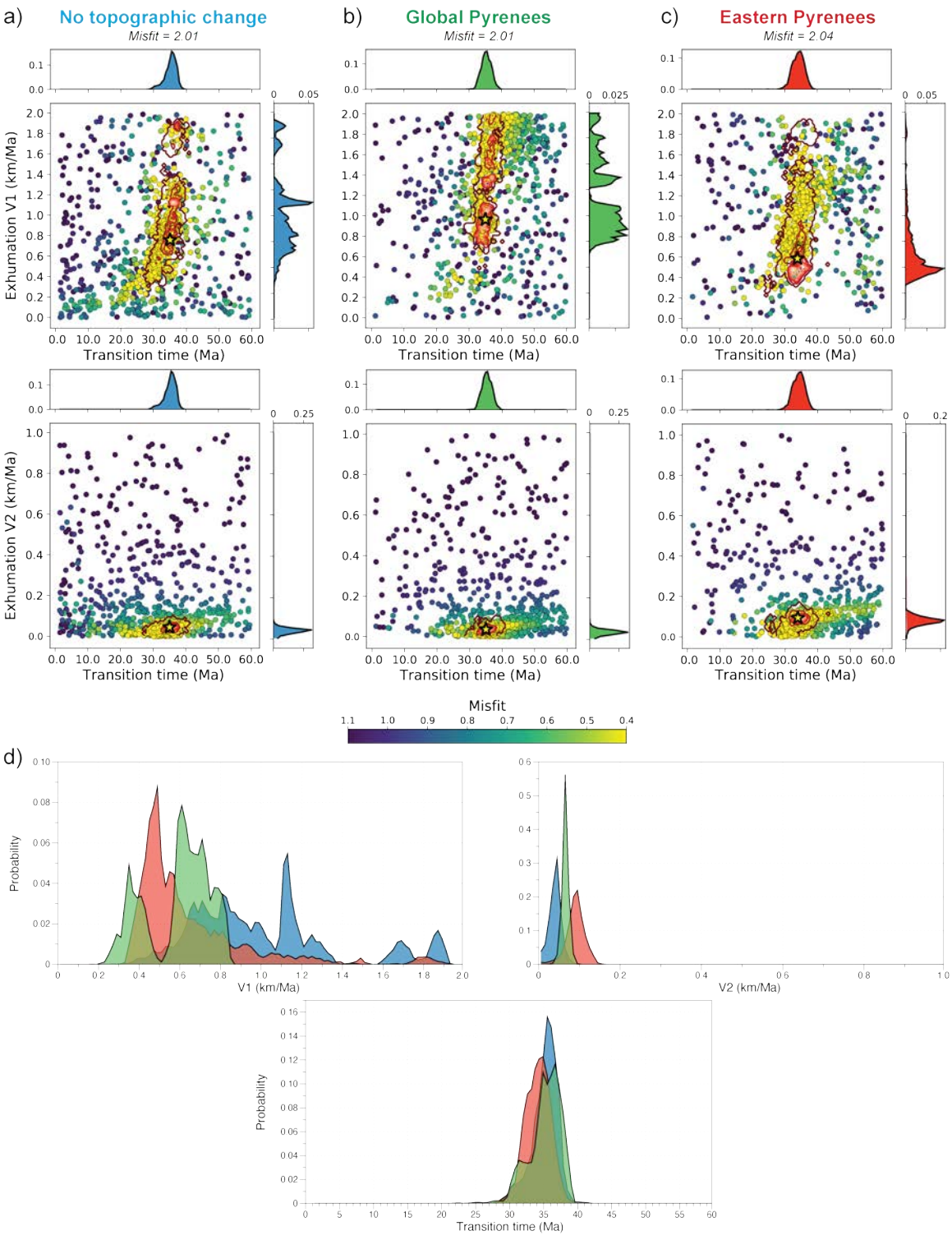

Figure 5. 3D Pecube inversion results for the South Mérens block, using the 3 TEMs: (a) No topographic change, (b) Global Pyrenees, (c) Eastern Pyrenees. In these model runs, 3 parameters are inverted: exhumation rates V1 and V2, and the transition time between the two exhumation phases. Scatter diagrams show results of Pecube and NA inversion with

746 the probability density function (PDF) adjacent to the axes for each parameter. Each dot
747 corresponds to a forward model; its color is proportional to the value of the reduced
748 misfit between model predictions and the observed low-T thermochronological data.
749 Note that violet corresponds to high misfits and yellow to low misfits. The yellow stars
750 are the best-fitting model (values given on top for each TEM). Red and black lines are 2D
751 posterior marginal probability density functions (PDFs) with 2σ (black) and 1σ (red)
752 confidence contours. d) Probability density function (PDF) results for the 3 inverted
753 parameters and three considered TEMs (blue: No topographic change, green: Global
754 Pyrenees, and red: Eastern Pyrenees).
755

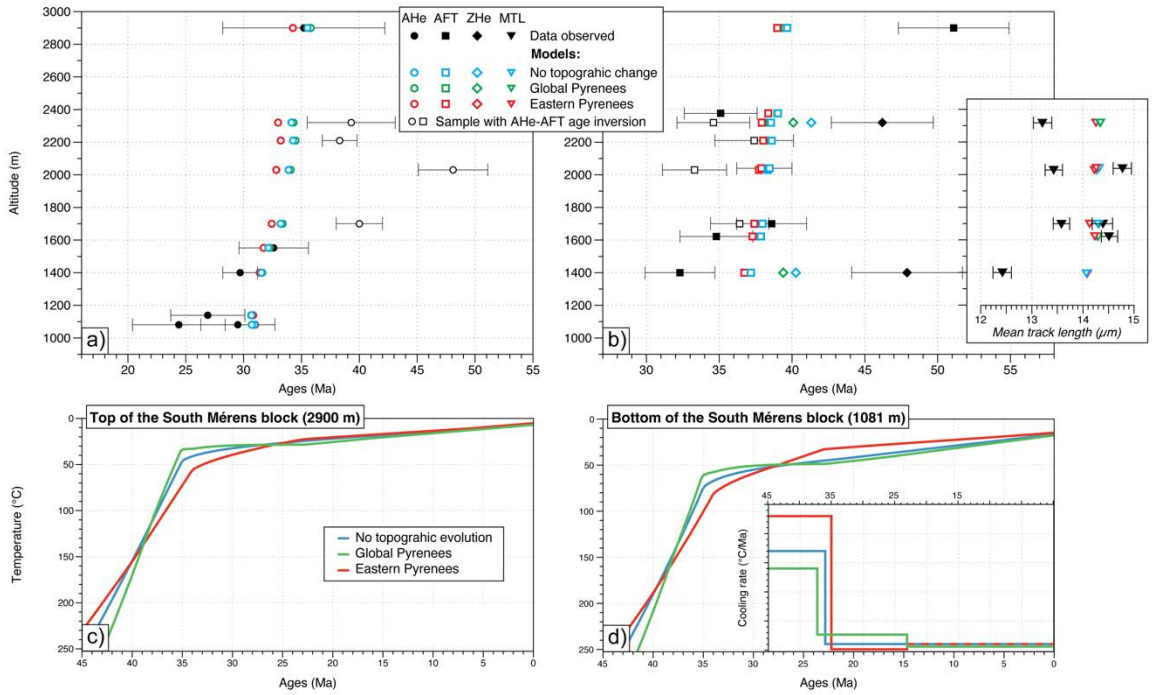

Figure 6. Age-elevation profiles with best-fitting predicted vs. observed AHe, AFT and ZHe ages and MTLs, and output thermal histories from the South Mérens block. a-b) Black dots (AHe, a), squares (AFT, b), diamonds (ZHe, b) and triangle (MTL, subplot in b) are observed data and associated uncertainties. Colored dots, squares, diamonds and triangles are predicted data for the 3 TEMs. c-d) Best-fitting output thermal histories for top (c) and bottom (d) samples of the South Mérens block, considering the 3 different TEMs. Inset plot shows the predicted cooling rates for the 3 TEMs.

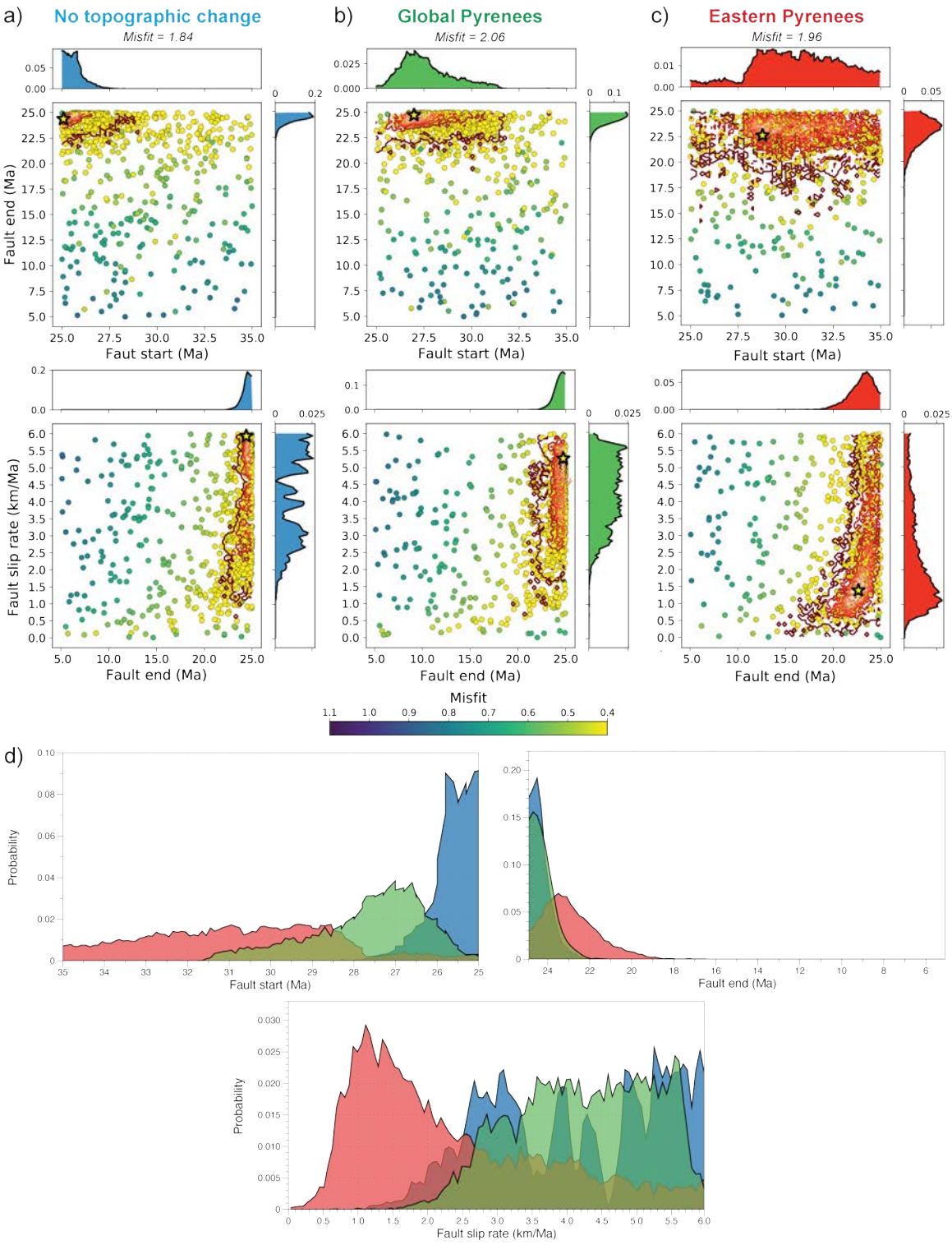

Figure 7. 3D Pecube inversion results of the Têt fault activity for the Canigou block, using the 3 TEMs: (a) No topographic change, (b) Global Pyrenees, (c) Eastern Pyrenees. In these model runs, 3 parameters are inverted: the Têt fault start and end times, and the slip rate on the fault. Scatter diagrams show results of Pecube and NA inversion with the probability density function (PDF) adjacent to the axes for each parameter. Each dot

770 corresponds to a forward model; its color is proportional to the value of the reduced
771 misfit between model predictions and the observed low-T thermochronological data.
772 Note that violet corresponds to high misfits and yellow to low misfits. The yellow stars
773 are the best-fitting model (values given on top for each TEM). Red and black lines are 2D
774 posterior marginal probability density functions (PDFs) with 2σ (black) and 1σ (red)
775 confidence contours. d) Probability density function (PDF) results for the 3 inverted
776 parameters and three considered TEMs (blue: No topographic change, green: Global
777 Pyrenees, and red: Eastern Pyrenees).

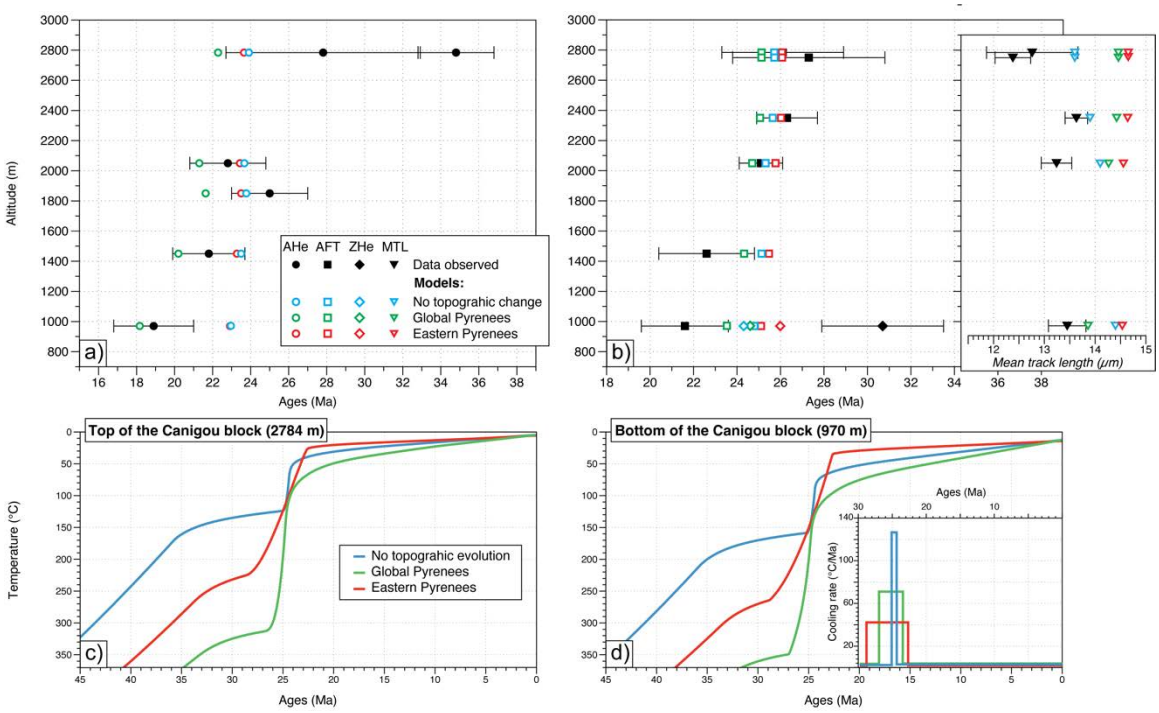

Figure 8. Age-elevation profile with best-fitting predicted vs. observed AHe, AFT and ZHe ages and MTLs, and output thermal histories from the Canigou block. a-b) Black dots (AHe, a), squares (AFT, b), diamonds (ZHe, b) and triangle (MTL, subplot in b) are observed data and associated uncertainties. Colored dots, squares, diamonds and triangles are predicted data for the 3 TEMs. c-d) Best-fitting output thermal histories for top (c) and bottom (d) samples of the Canigou block, considering the 3 different TEMs. Inset plot shows the predicted cooling rates for the 3 TEMs.

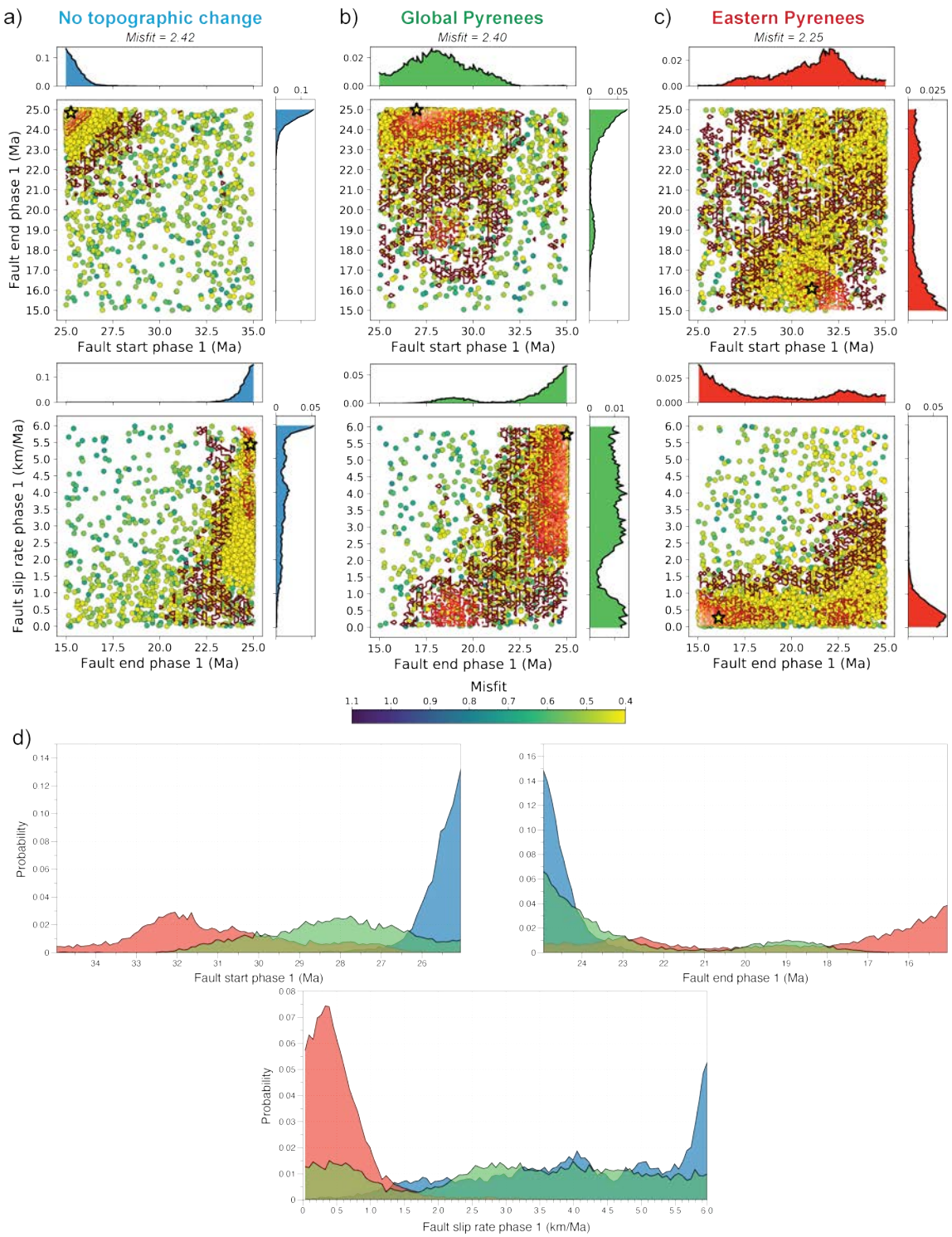

Figure 9. 3D Pecube inversion results of the first phase of the Têt fault activity for the Carança block, using the 3 TEMs: (a) No topographic change, (b) Global Pyrenees, (c) Eastern Pyrenees. In these model runs, 6 parameters are inverted: the Têt fault start and end times, and the slip rate on the fault for the 2 phases of fault activity. Scatter diagrams show results of Pecube and NA inversion with the probability density function (PDF)

adjacent to the axes for each parameter. Each dot corresponds to a forward model; its color is proportional to the value of the reduced misfit between model predictions and the observed low-T thermochronological data. Note that violet corresponds to high misfits and yellow to low misfits. The yellow stars are the best-fitting model (values given on top for each TEM). Red and black lines are 2D posterior marginal probability density functions (PDFs) with 2σ (black) and 1σ (red) confidence contours. d) Probability density function (PDF) results for the 3 inverted parameters and three considered TEMs (blue: No topographic change, green: Global Pyrenees, and red: Eastern Pyrenees).

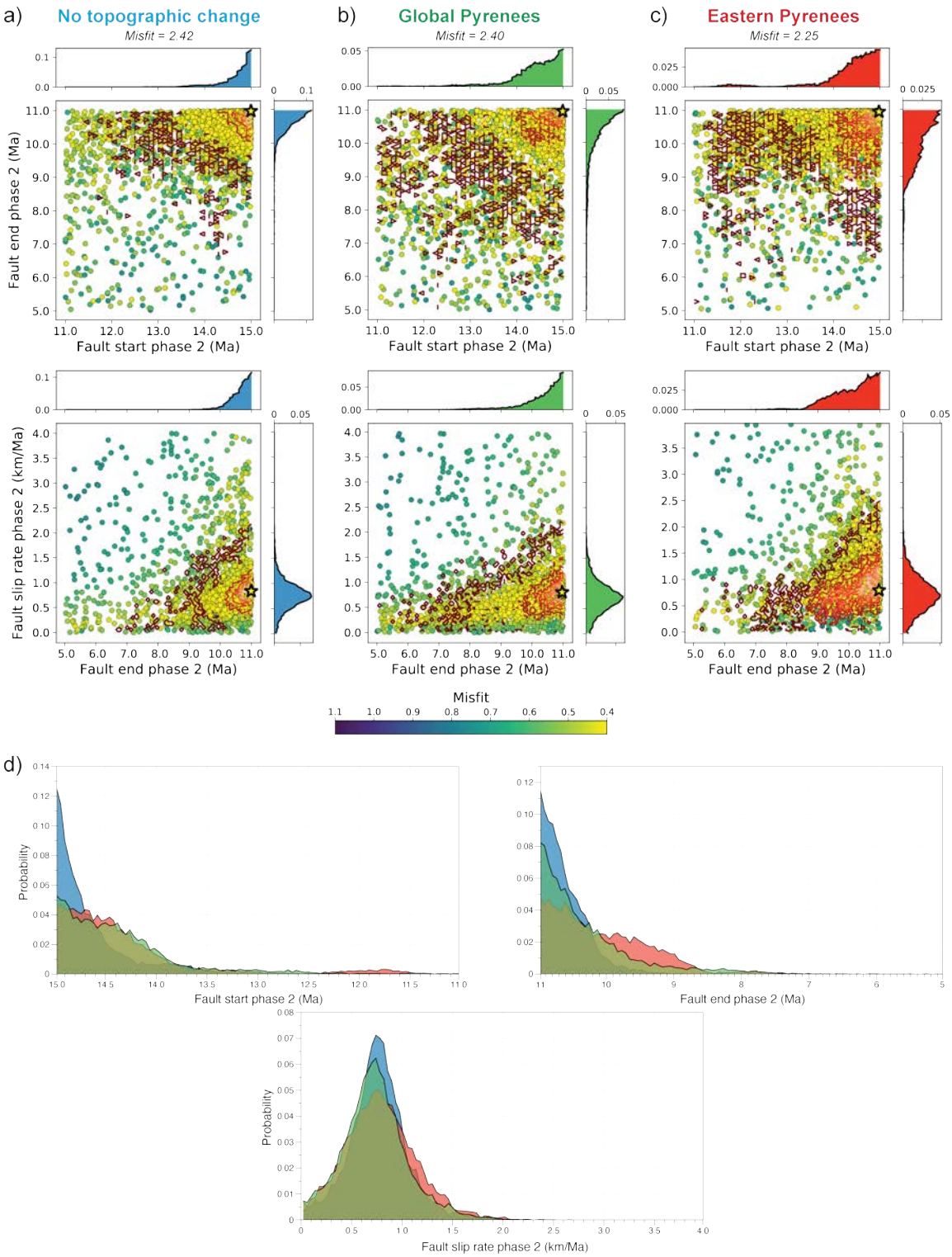

Figure 10. 3D Pecube inversion results of the second phase of the Têt fault activity, using the 3 TEMs for the Carança block: (a) No topographic change, (b) Global Pyrenees, and (c) Eastern Pyrenees. In these model runs, 6 parameters are inverted: the Têt fault start and end times, and the slip rate on the fault for the 2 phases of fault activity. Scatter diagrams show results of Pecube and NA inversion with the probability density function

(PDF) adjacent to the axes for each parameter. Each dot corresponds to a forward model; its color is proportional to the value of the reduced misfit between model predictions and the observed low-T thermochronological data. Note that violet corresponds to high misfits and to low misfits. The yellow stars are the best-fitting model (values given on top for each TEM). Red and black lines are 2D posterior marginal probability density functions (PDFs) with 2σ (black) and 1σ (red) confidence contours. d) Probability density function (PDF) results for the 3 inverted parameters and three considered TEMs (blue: No topographic change, green: Global Pyrenees, and red: Eastern Pyrenees).

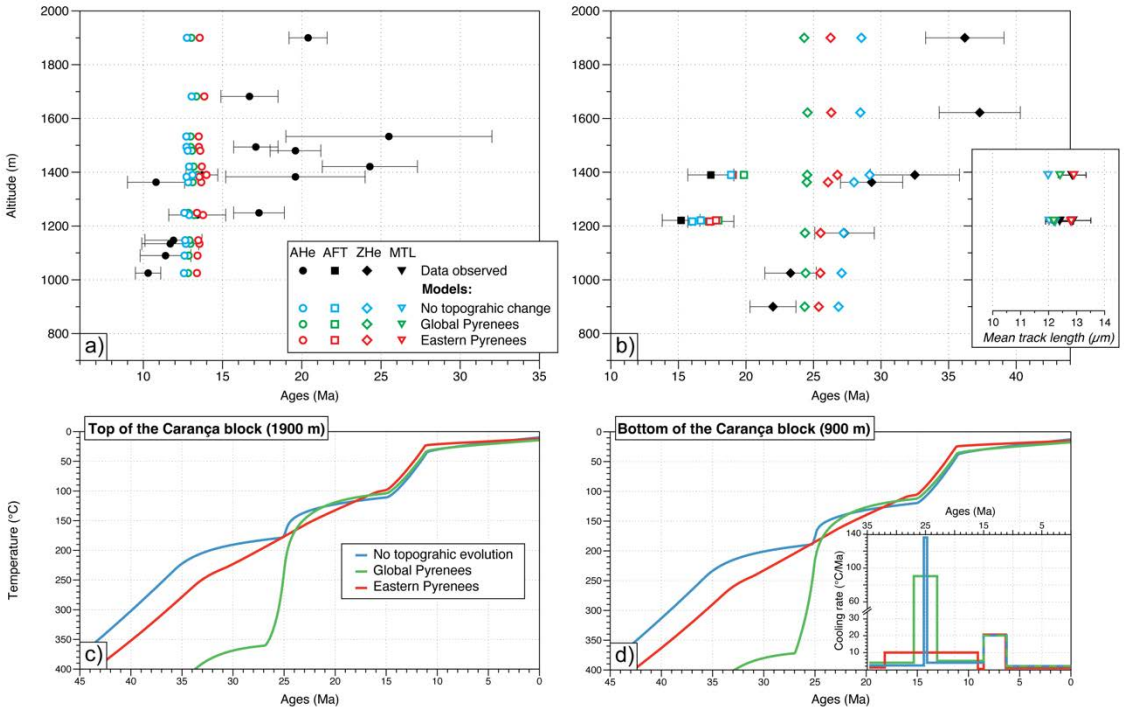

Figure 11. Age-elevation profiles with best-fitting predicted vs. observed AHe, AFT and ZHe ages and MTLs, and output thermal histories from the Carança block. a-b) Black dots (AHe, a), squares (AFT, b), diamonds (ZHe, b) and triangle (MTL, subplot in b) are observed data and associated uncertainties. Colored dots, squares, diamonds and triangles are predicted data for the 3 TEMs. c-d) Best-fitting output thermal histories for top (c) and bottom (d) samples of the Carança block, considering the 3 different TEMs. Inset plot shows the predicted cooling rates for the 3 TEMs.

823 Table 1. Synthesis of Pecube inversion results

Parameters	**Range**	**Pecube inversion results**		
		South Merens block		
		No topographic change	*Global Pyrenees*	*Eastern Pyrenees*
Transition time (Ma)	0-60	36.0 ± 1.5	37.0 ± 2.1	35.2 ± 1.8
V1 (km/Ma)	0-2	>0.5	>0.5	0.3-0.6
V2 (km/Ma)	0-1	0.04 ± 0.03	0.06 ± 0.01	0.09 ± 0.03
		Canigou block		
		No topographic change	*Global Pyrenees*	*Eastern Pyrenees*
Têt fault start (Ma)	25-35	26-25	28-26	>28
Têt fault end (Ma)	25-5	24.5	24.5	23.5 ± 1.5
Slip rate (km/Ma)	0-6	>1.0	>1.5	1.0 ± 0.5
		Carança block		
		No topographic change	*Global Pyrenees*	*Eastern Pyrenees*
Têt fault start phase 1 (Ma)	35-25	26-25	28.0 ± 2.0	32 ± 1.0
Têt fault end phase 1 (Ma)	25-15	25-24	25-24	15
Slip rate phase 1 (km/Ma)	0-6	5.5-6	-	<1.0
Têt fault start phase 2 (Ma)	11-15	15	15	15
Têt fault end phase 2 (Ma)	5-11	11	11	11
Slip rate phase 2 (km/Ma)	0-4	0.7 ± 0.2	0.7 ± 0.3	0.8 ± 0.4

824

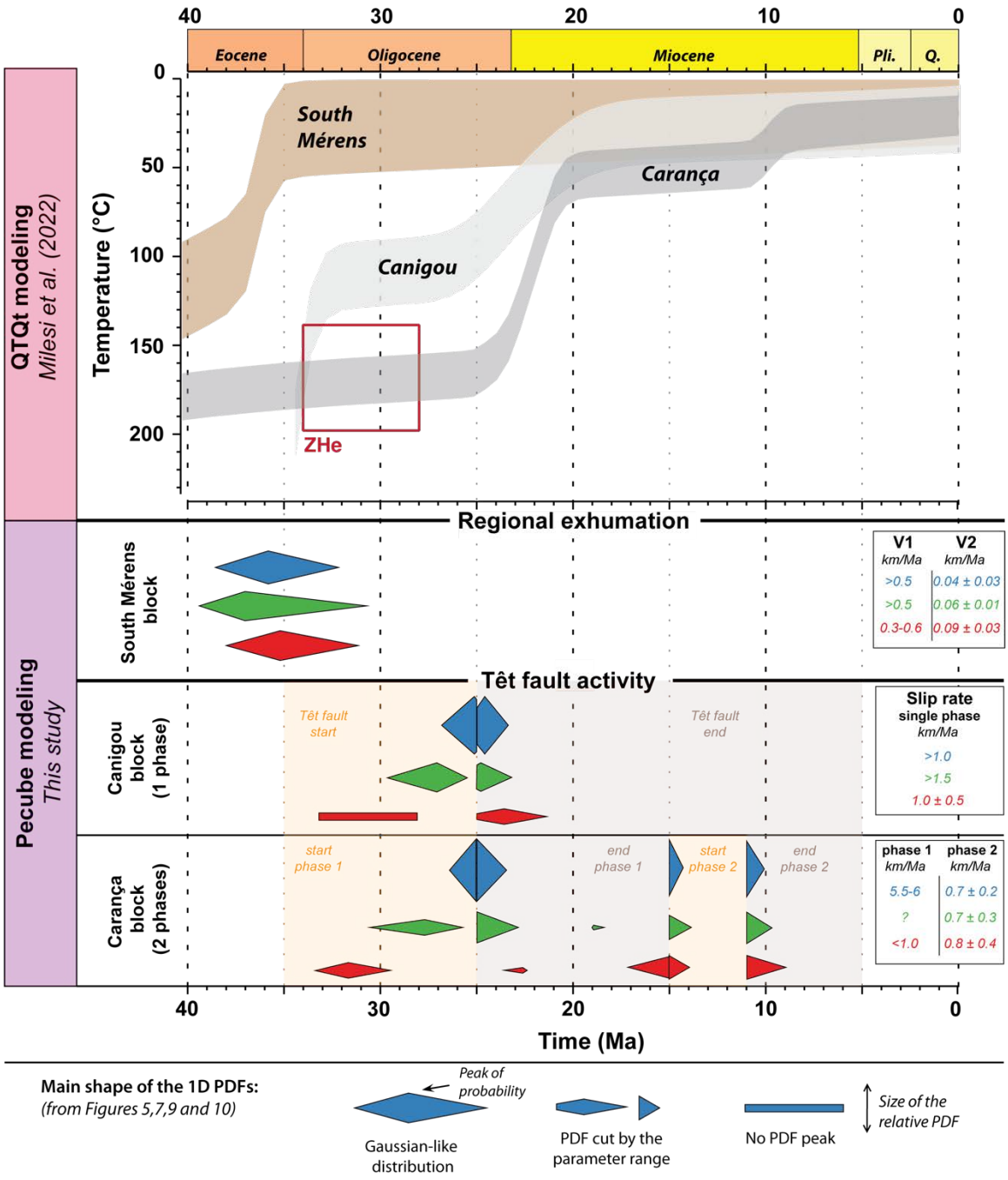

825

826 Figure 12. Summary results of QTQt thermal modeling (modified after Milesi et al.,
827 2022; red box indicates prescribed time-temperature constraint from ZHe data used in
828 QTQt modeling) and 3D Pecube inversions from this study, using 3 different TEMs
829 (blue: No topographic change, green: Global Pyrenees, and red: Eastern Pyrenees).
830 Diamonds schematically (see legend for details) represent the probability density
831 functions (PDFs) for the timing of the different exhumation or fault-activity phases: PDF
832 values >0.2 are considered for South Mérens inversion, and >0.1 for Canigou and
833 Carança inversions. Output exhumation and fault-slip rates are indicated (bottom right).

834 Time ranges explored for the start and the end of the Têt fault activity are indicated in
835 light orange and light grey colors, respectively.

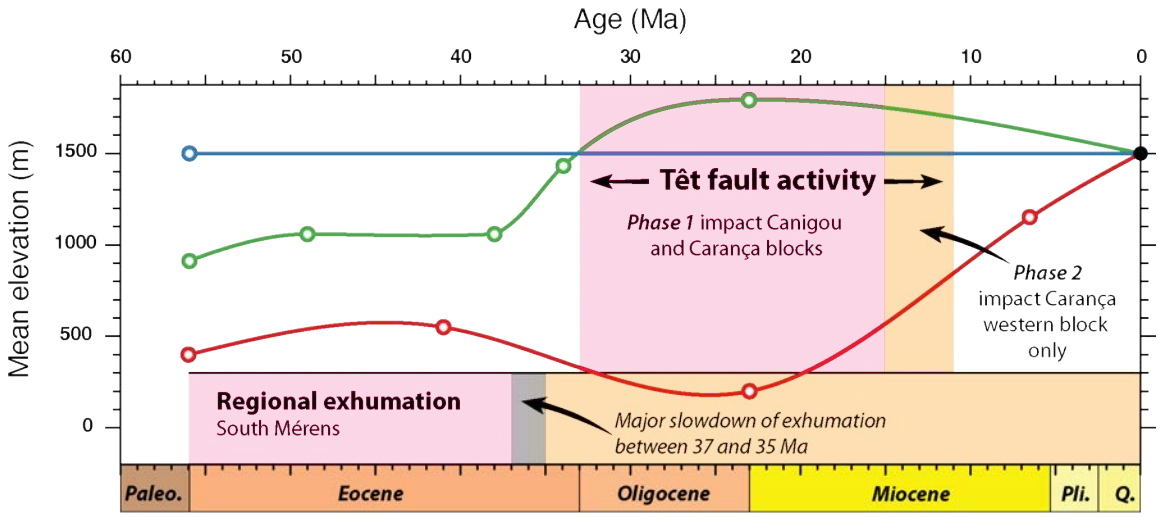

836

837 Figure 13. Summary information of the three topographic evolution models (TEMs) used
838 in Pecube thermo-kinematic modeling (blue: No topographic change; green: Global
839 Pyrenees; red: Eastern Pyrenees, see Section 3.3 for further details). The temporal
840 windows highlighted in light pink (i.e. 55-37 Ma for the regional exhumation and 33-15
841 Ma for the Têt fault activity) and light orange (i.e. 35-0 Ma for the regional exhumation
842 and 15-11 Ma for the Têt fault activity) represent divergent and convergent Pecube
843 inversion results (Fig. 12) between the different TEMs, respectively. See text for details.

REFERENCES

Agustí, J., Oms, O., Furió, M., Pérez-Vila, M.-J., & Roca, E. (2006). The Messinian terrestrial record in the Pyrenees : The case of Can Vilella (Cerdanya Basin). Palaeogeography, Palaeoclimatology, Palaeoecology, 238(1-4), 179-189. https://doi.org/10.1016/j.palaeo.2006.03.024

Angrand, P., & Mouthereau, F. (2021). Evolution of the Alpine orogenic belts in the Western Mediterranean region as resolved by the kinematics of the Europe-Africa diffuse plate boundary. BSGF - Earth Sciences Bulletin, 192, 42. https://doi.org/10.1051/bsgf/2021031

Avdievitch, N. N., Ehlers, T. A., & Glotzbach, C. (2018). Slow Long-Term Exhumation of the West Central Andean Plate Boundary, Chile. Tectonics, 37(7), 2243-2267. https://doi.org/10.1029/2017TC004944

Babault, J., Van Den Driessche, J., Bonnet, S., Castelltort, S., & Crave, A. (2005). Origin of the highly elevated Pyrenean peneplain : ORIGIN OF THE HIGHLY ELEVATED PYRENEAN. Tectonics, 24(2). https://doi.org/10.1029/2004TC001697

Bache, F., Olivet, J. L., Gorini, C., Aslanian, D., Labails, C., & Rabineau, M. (2010). Evolution of rifted continental margins : The case of the Gulf of Lions (Western Mediterranean Basin). Earth and Planetary Science Letters, 292(3-4), 345-356. https://doi.org/10.1016/j.epsl.2010.02.001

Batt, G. E., & Braun, J. (1997). On the thermomechanical evolution of compressional orogens. Geophysical Journal International, 128(2), 364-382. https://doi.org/10.1111/j.1365-246X.1997.tb01561.x

Beaumont, C. (1981). Foreland basins. Geophysical Journal International, 65(2), 291-329. https://doi.org/10.1111/j.1365-246X.1981.tb02715.x

Bermúdez, M. A., Velandia, F., García-Delgado, H., Jiménez, D., & Bernet, M. (2021). Exhumation of the southern transpressive Bucaramanga fault, eastern Cordillera of Colombia : Insights from detrital, quantitative thermochronology and geomorphology. Journal of South American Earth Sciences, 106, 103057. https://doi.org/10.1016/j.jsames.2020.103057

Bernard, T., Sinclair, H. D., Naylor, M., Christophoul, F., & Ford, M. (2021). Post-orogenic sediment drape in the Northern Pyrenees explained using a box model. Basin Research, 33(1), 118-137. https://doi.org/10.1111/bre.12457

Beucher, R., van der Beek, P., Braun, J., & Batt, G. E. (2012). Exhumation and relief development in the Pelvoux and Dora-Maira massifs (western Alps) assessed by spectral

877 analysis and inversion of thermochronological age transects : RELIEF EVOLUTION IN THE
878 WESTERN ALPS. Journal of Geophysical Research: Earth Surface, 117(F3).
879 https://doi.org/10.1029/2011JF002240
880 Bosch, G. V., Teixell, A., Jolivet, M., Labaume, P., Stockli, D., Domènech, M., & Monié, P.
881 (2016a). Timing of Eocene–Miocene thrust activity in the Western Axial Zone and Chaînons
882 Béarnais (west-central Pyrenees) revealed by multi-method thermochronology. Comptes
883 Rendus Geoscience, 348(3-4), 246-256. https://doi.org/10.1016/j.crte.2016.01.001
884 Bosch, G. V., Van Den Driessche, J., Babault, J., Robert, A., Carballo, A., Le Carlier, C., Loget,
885 N., Prognon, C., Wyns, R., & Baudin, T. (2016b). Peneplanation and lithosphere dynamics in
886 the Pyrenees. Comptes Rendus Geoscience, 348(3-4), 194-202.
887 https://doi.org/10.1016/j.crte.2015.08.005
888 Braun, J. (2003). Pecube : A new finite-element code to solve the 3D heat transport equation
889 including the effects of a time-varying, finite amplitude surface topography. Computers &
890 Geosciences, 29(6), 787-794. https://doi.org/10.1016/S0098-3004(03)00052-9
891 Braun, J., & Robert, X. (2005). Constraints on the rate of post-orogenic erosional decay from
892 low-temperature thermochronological data : Application to the Dabie Shan, China. Earth
893 Surface Processes and Landforms, 30(9), 1203□1225. https://doi.org/10.1002/esp.1271
894 Braun, J. (2010). The many surface expressions of mantle dynamics. Nature Geoscience, 3(12),
895 825-833. https://doi.org/10.1038/ngeo1020
896 Braun, J., van der Beek, P., Valla, P., Robert, X., Herman, F., Glotzbach, C., Pedersen, V., Perry,
897 C., Simon-Labric, T., & Prigent, C. (2012). Quantifying rates of landscape evolution and
898 tectonic processes by thermochronology and numerical modeling of crustal heat transport
899 using PECUBE. Tectonophysics, 524-525, 1-28. https://doi.org/10.1016/j.tecto.2011.12.035
900 Calvet, M., Gunnell, Y., & Delmas, M. (2014). The Têt River Valley : A Condensed Record of
901 Long-Term Landscape Evolution in the Pyrenees. In M. Fort & M.-F. André (Éds.),
902 Landscapes and Landforms of France (p. 127-138). Springer Netherlands.
903 https://doi.org/10.1007/978-94-007-7022-5_13
904 Calvet, M., Gunnell, Y., & Laumonier, B. (2021). Denudation history and palaeogeography of the
905 Pyrenees and their peripheral basins : An 84-million-year geomorphological perspective.
906 Earth-Science Reviews, 215, 103436. https://doi.org/10.1016/j.earscirev.2020.103436
907 Calvet, M. (1999). Régimes des contraintes et volumes de relief dans l'est des Pyrénées/stress
908 regimes and volumes of reliefs in the Eastern Pyrenees. Géomorphologie: Relief, Processus,
909 Environnement, 5(3), 253–278. https://doi.org/10.3406/morfo.1999.991

910 Capaldi, T. N., Odlum, M. L., Curry, M. E., & Stockli, D. F. (2022). Variable thermal histories
911 across the Pyrenees orogen recorded in modern river sand detrital geo-/thermochronology
912 and PECUBE thermokinematic modelling. Basin Research, 34(5), 1781-1806.
913 https://doi.org/10.1111/bre.12685
914 Carozza, J.-M., & Baize, S. (2004). L'escarpement de faille de la Têt est-il le résultat de la
915 tectonique active Plio-Pléistocène ou d'une exhumation Pléistocène ? Comptes Rendus
916 Geoscience, 336(3), 217-226. https://doi.org/10.1016/j.crte.2003.10.026
917 Carozza, J.-M., & Delcaillau, B. (1999). L'enregistrement géomorphologique de la tectonique
918 quaternaire par les nappes alluviales: L'exemple du bassin de la têt (roussillon, France).
919 Comptes Rendus de l'Academie des Sciences—Series IIA: Earth and Planetary Science,
920 329(10), 735–740. https://doi.org/10.1016/s1251-8050(00)88493-1
921 Cederbom, C. E., Sinclair, H. D., Schlunegger, F., & Rahn, M. K. (2004). Climate-induced
922 rebound and exhumation of the European Alps. Geology, 32(8), 709.
923 https://doi.org/10.1130/G20491.1
924 Chevrot, S., Sylvander, M., Diaz, J., Martin, R., Mouthereau, F., Manatschal, G., Masini, E.,
925 Calassou, S., Grimaud, F., Pauchet, H., & Ruiz, M. (2018). The non-cylindrical crustal
926 architecture of the Pyrenees. Scientific Reports, 8(1). https://doi.org/10.1038/s41598-018-
927 27889-x
928 Coney, P. J., Muñoz, J. A., McCLAY, K. R., & Evenchick, C. A. (1996). Syntectonic burial and
929 post-tectonic exhumation of the southern Pyrenees foreland fold–thrust belt. Journal of the
930 Geological Society, 153(1), 9-16. https://doi.org/10.1144/gsjgs.153.1.0009
931 Coutand, I., Whipp, D. M., Grujic, D., Bernet, M., Fellin, M. G., Bookhagen, B., Landry, K. R.,
932 Ghalley, S. K., & Duncan, C. (2014). Geometry and kinematics of the Main Himalayan
933 Thrust and Neogene crustal exhumation in the Bhutanese Himalaya derived from inversion of
934 multithermochronologic data : NEOGENE EXHUMATION OF BHUTAN HIMALAYAS.
935 Journal of Geophysical Research: Solid Earth, 119(2), 1446-1481.
936 https://doi.org/10.1002/2013JB010891
937 Cruset, D., Vergés, J., Albert, R., Gerdes, A., Benedicto, A., Cantarero, I., & Travé, A. (2020).
938 Quantifying deformation processes in the SE Pyrenees using U–Pb dating of fracture-filling
939 calcites. Journal of the Geological Society, 177(6), 1186-1196.
940 https://doi.org/10.1144/jgs2020-014
941 Curry, M. E., Beek, P. van der, Huismans, R. S., Wolf, S. G., Fillon, C., & Muñoz, J.-A. (2021).
942 Spatio-temporal patterns of Pyrenean exhumation revealed by inverse thermo-kinematic

943 modeling of a large thermochronologic data set. Geology, 49(6), 738-742.
944 https://doi.org/10.1130/G48687.1
945 Curry, M. E., van der Beek, P., Huismans, R. S., Wolf, S. G., & Muñoz, J.-A. (2019). Evolving
946 paleotopography and lithospheric flexure of the Pyrenean Orogen from 3D flexural modeling
947 and basin analysis. Earth and Planetary Science Letters, 515, 26-37.
948 https://doi.org/10.1016/j.epsl.2019.03.009
949 Dadson, S. J., Hovius, N., Chen, H., Dade, W. B., Hsieh, M.-L., Willett, S. D., Hu, J.-C., Horng,
950 M.-J., Chen, M.-C., Stark, C. P., Lague, D., & Lin, J.-C. (2003). Links between erosion,
951 runoff variability and seismicity in the Taiwan orogen. Nature, 426(6967), 648-651.
952 https://doi.org/10.1038/nature02150
953 Delcaillau, B., Carozza, J.-M., & Font, M. (2004). The northern segment of the Têt Fault
954 (Pyrenees-Orientales) : Neogene evolution and geomorphic implications. Bulletin de la
955 Société Géologique de France, 175(3), 257-272. https://doi.org/10.2113/175.3.257
956 Diaz, J., Vergés, J., Chevrot, S., Antonio-Vigil, A., Ruiz, M., Sylvander, M., & Gallart, J. (2018).
957 Mapping the crustal structure beneath the eastern Pyrenees. Tectonophysics, 744, 296-309.
958 https://doi.org/10.1016/j.tecto.2018.07.011
959 Ehlers, T. A., Armstrong, P. A., & Chapman, D. S. (2001). Normal fault thermal regimes and the
960 interpretation of low-temperature thermochronometers. Physics of the Earth and Planetary
961 Interiors, 126(3-4), 179-194. https://doi.org/10.1016/S0031-9201(01)00254-0
962 Ehlers, T. A., & Chapman, D. S. (1999). Normal fault thermal regimes : Conductive and
963 hydrothermal heat transfer surrounding the Wasatch fault, Utah. Tectonophysics, 312(2-4),
964 217-234. https://doi.org/10.1016/S0040-1951(99)00203-6
965 Ehlers, T. A., & Farley, K. A. (2003). Apatite (U–Th)/He thermochronometry : Methods and
966 applications to problems in tectonic and surface processes. Earth and Planetary Science
967 Letters, 206(1-2), 1-14. https://doi.org/10.1016/S0012-821X(02)01069-5
968 Erdős, Z., van der Beek, P., & Huismans, R. S. (2014). Evaluating balanced section restoration
969 with thermochronology data : A case study from the Central Pyrenees. Tectonics, 33(5),
970 617-634. https://doi.org/10.1002/2013TC003481
971 Farley, K. A. (2002). (U-Th)/He Dating : Techniques, Calibrations, and Applications. Reviews in
972 Mineralogy and Geochemistry, 47(1), 819-844. https://doi.org/10.2138/rmg.2002.47.18
973 Fillon, C., Mouthereau, F., Calassou, S., Pik, R., Bellahsen, N., Gautheron, C., Stockli, D.,
974 Brichau, S., Daril, N., Mouchené, M., & van der Beek, P. (2021). Post-orogenic exhumation
975 in the western Pyrenees : Evidence for extension driven by pre-orogenic inheritance. Journal
976 of the Geological Society, 178(2), jgs2020-079. https://doi.org/10.1144/jgs2020-079

977 Fillon, C., Pedreira, D., van der Beek, P. A., Huismans, R. S., Barbero, L., & Pulgar, J. A. (2016).
978 Alpine exhumation of the central Cantabrian Mountains, Northwest Spain : ALPINE
979 EXHUMATION OF THE CANTABRIANS. Tectonics, 35(2), 339-356.
980 https://doi.org/10.1002/2015TC004050
981 Fillon, C., & van der Beek, P. (2012). Post-orogenic evolution of the southern Pyrenees :
982 Constraints from inverse thermo-kinematic modelling of low-temperature thermochronology
983 data. Basin Research, 24(4), 418-436. https://doi.org/10.1111/j.1365-2117.2011.00533.x
984 Fitzgerald, P. G., Muñoz, J. A., Coney, P. J., & Baldwin, S. L. (1999). Asymmetric exhumation
985 across the Pyrenean orogen : Implications for the tectonic evolution of a collisional orogen.
986 Earth and Planetary Science Letters, 173(3), 157-170. https://doi.org/10.1016/S0012-
987 821X(99)00225-3
988 Fletcher, J. M., Kohn, B. P., Foster, D. A., & Gleadow, A. J. (2000). Heterogeneous Neogene
989 cooling and exhumation of the Los Cabos block, southern Baja California: Evidence from
990 fission-track thermochronology. Geology, 28(2), 107-110. https://doi.org/10.1130/0091-
991 7613(2000)28<107:HNCAEO>2.0.CO;2
992 Foeken, J. P. T., Persano, C., Stuart, F. M., & ter Voorde, M. (2007). Role of topography in
993 isotherm perturbation : Apatite (U-Th)/He and fission track results from the Malta tunnel,
994 Tauern Window, Austria: TOPOGRAPHY AND ISOTHERMS. Tectonics, 26(3).
995 https://doi.org/10.1029/2006TC002049
996 Ford, M., Masini, E., Vergés, J., Pik, R., Ternois, S., Léger, J., Dielforder, A., Frasca, G., Grool,
997 A., Vinciguerra, C., Bernard, T., Angrand, P., Crémades, A., Manatschal, G., Chevrot, S.,
998 Jolivet, L., Mouthereau, F., Thinon, I., & Calassou, S. (2022). Evolution of a low
999 convergence collisional orogen : A review of Pyrenean orogenesis. BSGF - Earth Sciences
1000 Bulletin, 193, 19. https://doi.org/10.1051/bsgf/2022018
1001 Gautheron, C., Tassan-Got, L., Barbarand, J., & Pagel, M. (2009). Effect of alpha-damage
1002 annealing on apatite (U–Th)/He thermochronology. Chemical Geology, 266(3-4), 157-170.
1003 https://doi.org/10.1016/j.chemgeo.2009.06.001
1004 Gérard, B., Robert, X., Audin, L., Valla, P. G., Bernet, M., & Gautheron, C. (2021). Differential
1005 Exhumation of the Eastern Cordillera in the Central Andes : Evidence for South - Verging
1006 Backthrusting (Abancay Deflection, Peru). Tectonics, 40(4).
1007 https://doi.org/10.1029/2020TC006314
1008 Gibson, M., Sinclair, H. D., Lynn, G. J., & Stuart, F. M. (2007). Late- to post-orogenic
1009 exhumation of the Central Pyrenees revealed through combined thermochronological data

and modelling. Basin Research, 19(3), 323-334. https://doi.org/10.1111/j.1365-2117.2007.00333.x

Glotzbach, C., van der Beek, P. A., & Spiegel, C. (2011). Episodic exhumation and relief growth in the Mont Blanc massif, Western Alps from numerical modelling of thermochronology data. Earth and Planetary Science Letters, 304(3-4), 417-430. https://doi.org/10.1016/j.epsl.2011.02.020

Grujic, D., Ashley, K. T., Coble, M. A., Coutand, I., Kellett, D. A., Larson, K. P., Whipp, D. M., Gao, M., & Whynot, N. (2020). Deformational Temperatures Across the Lesser Himalayan Sequence in Eastern Bhutan and Their Implications for the Deformation History of the Main Central Thrust. Tectonics, 39(4). https://doi.org/10.1029/2019TC005914

Gunnell, Y., Calvet, M., Brichau, S., Carter, A., Aguilar, J.-P., & Zeyen, H. (2009). Low long-term erosion rates in high-energy mountain belts : Insights from thermo- and biochronology in the Eastern Pyrenees. Earth and Planetary Science Letters, 278(3-4), 208-218. https://doi.org/10.1016/j.epsl.2008.12.004

Gunnell, Y., Zeyen, H., & Calvet, M. (2008). Geophysical evidence of a missing lithospheric root beneath the Eastern Pyrenees : Consequences for post-orogenic uplift and associated geomorphic signatures. Earth and Planetary Science Letters, 276(3-4), 302-313. https://doi.org/10.1016/j.epsl.2008.09.031

Herman, F., Seward, D., Valla, P. G., Carter, A., Kohn, B., Willett, S. D., & Ehlers, T. A. (2013). Worldwide acceleration of mountain erosion under a cooling climate. Nature, 504(7480), 423-426. https://doi.org/10.1038/nature12877

Huyghe, D., Mouthereau, F., & Emmanuel, L. (2012). Oxygen isotopes of marine mollusc shells record Eocene elevation change in the Pyrenees. Earth and Planetary Science Letters, 345-348, 131-141. https://doi.org/10.1016/j.epsl.2012.06.035

Huyghe, D., Mouthereau, F., & Emmanuel, L. (2012). Oxygen isotopes of marine mollusc shells record Eocene elevation change in the Pyrenees. Earth and Planetary Science Letters, 345-348, 131-141. https://doi.org/10.1016/j.epsl.2012.06.035

Huyghe, D., Mouthereau, F., Sébilo, M., Vacherat, A., Ségalen, L., Richard, P., Biron, P., & Bariac, T. (2018). Impact of topography, climate and moisture sources on isotopic composition (δ18O & δD) of rivers in the Pyrenees : Implications for topographic reconstructions in small orogens. Earth and Planetary Science Letters, 484, 370-384. https://doi.org/10.1016/j.epsl.2017.12.035

Huyghe, D., Mouthereau, F., Ségalen, L., & Furió, M. (2020). Long-term dynamic topographic support during post-orogenic crustal thinning revealed by stable isotope (δ18O) paleo-

altimetry in eastern Pyrenees. Scientific Reports, 10(1). https://doi.org/10.1038/s41598-020-58903-w

Jamieson, R. A., & Beaumont, C. (2013). On the origin of orogens. Geological Society of America Bulletin, 125(11-12), 1671-1702. https://doi.org/10.1130/B30855.1

Jolivet, L., Baudin, T., Calassou, S., Chevrot, S., Ford, M., Issautier, B., Lasseur, E., Masini, E., Manatschal, G., Mouthereau, F., Thinon, I., & Vidal, O. (2021). Geodynamic evolution of a wide plate boundary in the Western Mediterranean, near-field versus far-field interactions. BSGF - Earth Sciences Bulletin, 192, 48. https://doi.org/10.1051/bsgf/2021043

Jolivet, L., Romagny, A., Gorini, C., Maillard, A., Thinon, I., Couëffé, R., Ducoux, M., & Séranne, M. (2020). Fast dismantling of a mountain belt by mantle flow : Late-orogenic evolution of Pyrenees and Liguro-Provençal rifting. Tectonophysics, 776, 228312. https://doi.org/10.1016/j.tecto.2019.228312

Jolivet, M., Labaume, P., Monié, P., Brunel, M., Arnaud, N., & Campani, M. (2007). Thermochronology constraints for the propagation sequence of the south Pyrenean basement thrust system (France-Spain) : PROPAGATION OF THE SOUTH PYRENEAN PRISM. Tectonics, 26(5). https://doi.org/10.1029/2006TC002080

Labaume, P., Meresse, F., Jolivet, M., Teixell, A., & Lahfid, A. (2016). Tectonothermal history of an exhumed thrust-sheet-top basin : An example from the south Pyrenean thrust belt: JACA THRUST-SHEET-TOP BASIN. Tectonics, 35(5), 1280-1313. https://doi.org/10.1002/2016TC004192

Lanari, R., Boutoux, A., Faccenna, C., Herman, F., Willett, S. D., & Ballato, P. (2023). Cenozoic exhumation in the Mediterranean and the Middle East. Earth-Science Reviews, 104328. https://doi.org/10.1016/j.earscirev.2023.104328

Laumonier, B. (2015). Les Pyrénées alpines sud-orientales (France, Espagne) – essai de synthèse. Revue de Géologie pyrénéenne 2015(2), 44.

Maillard, A., Jolivet, L., Lofi, J., Thinon, I., Couëffé, R., Canva, A., & Dofal, A. (2020). Transfer zones and associated volcanic province in the eastern Valencia Basin : Evidence for a hot rifted margin? Marine and Petroleum Geology, 119, 104419. https://doi.org/10.1016/j.marpetgeo.2020.104419

Mancktelow, N. S., & Grasemann, B. (1997a). Time-dependent effects of heat advection and topography on cooling histories during erosion. Tectonophysics, 270(3-4), 167-195. https://doi.org/10.1016/S0040-1951(96)00279-X

1076 Mancktelow, N. S., & Grasemann, B. (1997b). Time-dependent effects of heat advection and
1077 topography on cooling histories during erosion. Tectonophysics, 270(3-4), 167-195.
1078 https://doi.org/10.1016/S0040-1951(96)00279-X
1079 Mauffret, A., Durand de Grossouvre, B., Tadeu Dos Reis, A., Gorini, C., & Nercessian, A.
1080 (2001). Structural geometry in the eastern Pyrenees and western Gulf of Lion (Western
1081 Mediterranean). Journal of Structural Geology, 23(11), 1701-1726.
1082 https://doi.org/10.1016/S0191-8141(01)00025-6
1083 Maurel, O., Brunel, M., & Monié, P. (2002). Exhumation cénozoïque des massifs du Canigou et
1084 de Mont-Louis (Pyrénées orientales, France). Comptes Rendus Geoscience, 334(12), 941-
1085 948. https://doi.org/10.1016/S1631-0713(02)01834-5
1086 Maurel, O., Moniè, P., Pik, R., Arnaud, N., Brunel, M., & Jolivet, M. (2008). The Meso-Cenozoic
1087 thermo-tectonic evolution of the Eastern Pyrenees: An 40Ar/39Ar fission track and (U–
1088 Th)/He thermochronological study of the Canigou and Mont-Louis massifs. International
1089 Journal of Earth Sciences, 97(3), 565-584. https://doi.org/10.1007/s00531-007-0179-x
1090 Metcalf, J. R., Fitzgerald, P. G., Baldwin, S. L., & Muñoz, J.-A. (2009). Thermochronology of a
1091 convergent orogen : Constraints on the timing of thrust faulting and subsequent exhumation
1092 of the Maladeta Pluton in the Central Pyrenean Axial Zone. Earth and Planetary Science
1093 Letters, 287(3-4), 488-503. https://doi.org/10.1016/j.epsl.2009.08.036
1094 Milesi, G., Soliva, R., Monié, P., Münch, P., Bellanger, M., Bruguier, O., Bonno, M., Taillefer,
1095 A., & Mayolle, S. (2019). Mapping a geothermal anomaly using apatite (U‐Th)/He
1096 thermochronology in the Têt fault damage zone, eastern Pyrenees, France. Terra Nova, 31(6),
1097 569-576. https://doi.org/10.1111/ter.12429
1098 Milesi, G. (2020). Analyse thermochronologique, géochimique et structurale du système
1099 hydrothermal de la faille de la Têt (Pyrénées, France), un nouvel outil d'exploration
1100 géothermique (PhD thesis). Université de Montpellier. https://theses.hal.science/tel-03180178
1101 Milesi, G., Monié, P., Soliva, R., Mûnch, P., Taillefer, A., Bellanger, M., et al. (2020a). Imaging
1102 geothermal anomalies using low-temperature (U-Th)/He thermochronometry: A case study
1103 from the active Têt fault hydrothermal system (Eastern Pyrenees, France). In Proceedings
1104 World Geothermal Congress 2020 Reykjavik, Iceland. 26 April to 2 May 2020.
1105 Milesi, G., Monié, P., Münch, P., Soliva, R., Taillefer, A., Bruguier, O., Bellanger, M., Bonno,
1106 M., & Martin, C. (2020b). Tracking geothermal anomalies along a crustal fault using (U −
1107 Th)/He apatite thermochronology and rare-earth element (REE) analyses : The example of the
1108 Têt fault (Pyrenees, France). Solid Earth, 11(5), 1747-1771. https://doi.org/10.5194/se-11-
1109 1747-2020

1110 Milesi, G., Monié, P., Soliva, R., Münch, P., Valla, P. G., Brichau, S., Bonno, M., Martin, C., &
1111 Bellanger, M. (2022). Deciphering the Cenozoic Exhumation History of the Eastern Pyrenees
1112 Along a Crustal-Scale Normal Fault Using Low-Temperature Thermochronology.
1113 Tectonics, 41(4). https://doi.org/10.1029/2021TC007172
1114 Monod, B., Regard, V., Carcone, J., Wyns, R., & Christophoul, F. (2016). Postorogenic planar
1115 palaeosurfaces of the central Pyrenees : Weathering and neotectonic records. Comptes
1116 Rendus Geoscience, 348(3-4), 184-193. https://doi.org/10.1016/j.crte.2015.09.005
1117 Mouthereau, F., Angrand, P., Jourdon, A., Ternois, S., Fillon, C., Calassou, S., Chevrot, S., Ford,
1118 M., Jolivet, L., Manatschal, G., Masini, E., Thinon, I., Vidal, O., & Baudin, T. (2021).
1119 Cenozoic mountain building and topographic evolution in Western Europe : Impact of
1120 billions of years of lithosphere evolution and plate kinematics. BSGF - Earth Sciences
1121 Bulletin, 192, 56. https://doi.org/10.1051/bsgf/2021040
1122 Mouthereau, F., Filleaudeau, P.-Y., Vacherat, A., Pik, R., Lacombe, O., Fellin, M. G., Castelltort,
1123 S., Christophoul, F., & Masini, E. (2014). Placing limits to shortening evolution in the
1124 Pyrenees : Role of margin architecture and implications for the Iberia/Europe convergence:
1125 Plate convergence in the Pyrenees. Tectonics, 33(12), 2283-2314.
1126 https://doi.org/10.1002/2014TC003663
1127 Muñoz, J. A. (1992). Evolution of a continental collision belt: ECORS-Pyrenees crustal balanced
1128 cross-section. Thrust tectonics, 235-246. https://doi.org/10.1007/978-94-011-3066-0_21
1129 Muñoz, J. A. (2019). Alpine Orogeny : Deformation and Structure in the Northern Iberian Margin
1130 (Pyrenees s.l.). In C. Quesada & J. T. Oliveira (Éds.), The Geology of Iberia : A Geodynamic
1131 Approach (p. 433-451). Springer International Publishing. https://doi.org/10.1007/978-3-030-
1132 11295-0_9
1133 Pitard, P., Replumaz, A., Chevalier, M. -L., Leloup, P. -H., Bai, M., Doin, M. -P., Thieulot, C.,
1134 Ou, X., Balvay, M., & Li, H. (2021). Exhumation History Along the Muli Thrust—
1135 Implication for Crustal Thickening Mechanism in Eastern Tibet. Geophysical Research
1136 Letters, 48(14). https://doi.org/10.1029/2021GL093677
1137 Pous, J., Julià, R., & Sugrañes, L. S. (1986). Cerdanya basin geometry and its implication on the
1138 neocene evolution of the Eastern Pyrenees. Tectonophysics, 129(1–4), 355–365.
1139 https://doi.org/10.1016/0040-1951(86)90261-1
1140 Puigdefàbregas, C., Muñoz, J. A., & Vergés, J. (1992). Thrusting and foreland basin evolution in
1141 the Southern Pyrenees. In K. R. McClay (Éd.), Thrust Tectonics (p. 247-254). Springer
1142 Netherlands. https://doi.org/10.1007/978-94-011-3066-0_22

1143 Rat, J., Mouthereau, F., Brichau, S., Vacherat, A., Fillon, C., & Gautheron, C. (2022). Timing and
1144 distribution of exhumation in the Ebro basin reveal a plate-scale 10 Ma geodynamic event.
1145 Global and Planetary Change, 218, 103973. https://doi.org/10.1016/j.gloplacha.2022.103973
1146 Réhault, J., Moussat, E., & Fabbri, A. (1987). Structural evolution of the Tyrrhenian back-arc
1147 basin. Marine Geology, 74(1–2), 123–150. https://doi.org/10.1016/0025-3227(87)90010-7
1148 Roca, E., & Desegaulx, P. (1992). Analysis of the geological evolution and vertical movements in
1149 the Valencia trough area, western mediterranean. Marine and Petroleum Geology, 9(2), 167–
1150 176. https://doi.org/10.1016/0264-8172(92)90089-w
1151 Romagny, A., Jolivet, L., Menant, A., Bessière, E., Maillard, A., Canva, A., Gorini, C., & Augier,
1152 R. (2020). Detailed tectonic reconstructions of the Western Mediterranean region for the last
1153 35 Ma, insights on driving mechanisms. BSGF - Earth Sciences Bulletin, 191, 37.
1154 https://doi.org/10.1051/bsgf/2020040
1155 Roure, F., Choukroune, P., Berastegui, X., Munoz, J. A., Villien, A., Matheron, P., Bareyt, M.,
1156 Seguret, M., Camara, P., & Deramond, J. (1989). Ecors deep seismic data and balanced cross
1157 sections : Geometric constraints on the evolution of the Pyrenees. Tectonics, 8(1), 41-50.
1158 https://doi.org/10.1029/TC008i001p00041
1159 Rushlow, C. R., Barnes, J. B., Ehlers, T. A., & Vergés, J. (2013). Exhumation of the southern
1160 Pyrenean fold-thrust belt (Spain) from orogenic growth to decay : EXHUMATION OF THE
1161 SOUTHERN PYRENEES. Tectonics, 32(4). https://doi.org/10.1002/tect.20030
1162 Sambridge, M. (1999a). Geophysical inversion with a neighbourhood algorithm—I. Searching a
1163 parameter space. Geophysical Journal International, 138(2), 479-494.
1164 https://doi.org/10.1046/j.1365-246X.1999.00876.x
1165 Sambridge, M. (1999b). Geophysical inversion with a neighbourhood algorithm—II. Appraising
1166 the ensemble. Geophysical Journal International, 138(3), 727-746.
1167 https://doi.org/10.1046/j.1365-246x.1999.00900.x
1168 Schildgen, T. F., Ehlers, T. A., Whipp, D. M., van Soest, M. C., Whipple, K. X., & Hodges, K. V.
1169 (2009). Quantifying canyon incision and Andean Plateau surface uplift, southwest Peru : A
1170 thermochronometer and numerical modeling approach. Journal of Geophysical Research,
1171 114(F4), F04014. https://doi.org/10.1029/2009JF001305
1172 Schildgen, T. F., van der Beek, P. A., D'Arcy, M., Roda-Boluda, D., Orr, E. N., & Wittmann, H.
1173 (2022). Quantifying drainage-divide migration from orographic rainfall over geologic
1174 timescales : Sierra de Aconquija, southern Central Andes. Earth and Planetary Science
1175 Letters, 579, 117345. https://doi.org/10.1016/j.epsl.2021.117345

1176 Séranne, M., Couëffé, R., Husson, E., Baral, C., & Villard, J. (2021). The transition from
1177 Pyrenean shortening to Gulf of Lion rifting in Languedoc (South France) – A tectonic-
1178 sedimentation analysis. BSGF - Earth Sciences Bulletin, 192, 27.
1179 https://doi.org/10.1051/bsgf/2021017
1180 Séranne, M. (1999). The Gulf of Lion continental margin (NW Mediterranean) revisited by IBS :
1181 An overview. Geological Society, London, Special Publications, 156(1), 15-36.
1182 https://doi.org/10.1144/GSL.SP.1999.156.01.03
1183 Shen, X., Braun, J., & Yuan, X. (2022). Southeastern margin of the Tibetan Plateau stopped
1184 expanding in the late Miocene. Earth and Planetary Science Letters, 583, 117446.
1185 https://doi.org/10.1016/j.epsl.2022.117446
1186 Sibuet, J.-C., Srivastava, S. P., & Spakman, W. (2004). Pyrenean orogeny and plate kinematics :
1187 PYRENEAN OROGENY AND PLATE KINEMATICS. Journal of Geophysical Research:
1188 Solid Earth, 109(B8). https://doi.org/10.1029/2003JB002514
1189 Sinclair, H. D., Gibson, M., Naylor, M., & Morris, R. G. (2005). Asymmetric growth of the
1190 Pyrenees revealed through measurement and modeling of orogenic fluxes. American Journal
1191 of Science, 305(5), 369-406. https://doi.org/10.2475/ajs.305.5.369
1192 Stüwe, K., White, L., & Brown, R. (1994). The influence of eroding topography on steady-state
1193 isotherms. Application to fission track analysis. Earth and Planetary Science Letters,
1194 124(1-4), 63-74. https://doi.org/10.1016/0012-821X(94)00068-9
1195 Suc, J.-P., & Fauquette, S. (2012). The use of pollen floras as a tool to estimate palaeoaltitude of
1196 mountains : The eastern Pyrenees in the Late Neogene, a case study. Palaeogeography,
1197 Palaeoclimatology, Palaeoecology, 321-322, 41-54.
1198 https://doi.org/10.1016/j.palaeo.2012.01.014
1199 Taillefer, A., Soliva, R., Guillou-Frottier, L., Le Goff, E., Martin, G., & Seranne, M. (2017).
1200 Fault-Related Controls on Upward Hydrothermal Flow: An Integrated Geological Study of
1201 the Têt Fault System, Eastern Pyrénées (France). Geofluids, 2017, 1-19.
1202 https://doi.org/10.1155/2017/8190109
1203 Taillefer, A., Milesi, G., Soliva, R., Monnier, L., Delorme, P., Guillou-Frottier, L., & Le Goff, E.
1204 (2021). Polyphased brittle deformation around a crustal fault : A multi-scale approach based
1205 on remote sensing and field data on the mountains surrounding the Têt hydrothermal system
1206 (Eastern Pyrénées, France). Tectonophysics, 804, 228710.
1207 https://doi.org/10.1016/j.tecto.2020.228710

1208 Teixell, A., Labaume, P., & Lagabrielle, Y. (2016). The crustal evolution of the west-central
1209 Pyrenees revisited : Inferences from a new kinematic scenario. Comptes Rendus Geoscience,
1210 348(3□4), 257□267. https://doi.org/10.1016/j.crte.2015.10.010
1211 Teixell, A., Labaume, P., Ayarza, P., Espurt, N., de Saint Blanquat, M., & Lagabrielle, Y. (2018).
1212 Crustal structure and evolution of the Pyrenean-Cantabrian belt : A review and new
1213 interpretations from recent concepts and data. Tectonophysics, 724-725, 146-170.
1214 https://doi.org/10.1016/j.tecto.2018.01.009
1215 Ternois, S., Odlum, M., Ford, M., Pik, R., Stockli, D., Tibari, B., Vacherat, A., & Bernard, V.
1216 (2019). Thermochronological Evidence of Early Orogenesis, Eastern Pyrenees, France.
1217 Tectonics, 38(4), 1308-1336. https://doi.org/10.1029/2018TC005254
1218 Ternois, S., Mouthereau, F., & Jourdon, A. (2021). Decoding low-temperature thermochronology
1219 signals in mountain belts : Modelling the role of rift thermal imprint into continental
1220 collision. BSGF - Earth Sciences Bulletin, 192, 38. https://doi.org/10.1051/bsgf/2021028
1221 Thieulot, C., Steer, P., & Huismans, R. S. (2014). Three-dimensional numerical simulations of
1222 crustal systems undergoing orogeny and subjected to surface processes. Geochemistry,
1223 Geophysics, Geosystems, 15(12), 4936-4957. https://doi.org/10.1002/2014GC005490
1224 Tosal, A., Verduzco, O., & Martín-Closas, C. (2021). CLAMP-based palaeoclimatic analysis of
1225 the late Miocene (Tortonian) flora from La Cerdanya Basin of Catalonia, Spain, and an
1226 estimation of the palaeoaltitude of the eastern Pyrenees. Palaeogeography,
1227 Palaeoclimatology, Palaeoecology, 564, 110186.
1228 https://doi.org/10.1016/j.palaeo.2020.110186
1229 Vacherat, A., Mouthereau, F., Pik, R., Bellahsen, N., Gautheron, C., Bernet, M., Daudet, M.,
1230 Balansa, J., Tibari, B., Pinna Jamme, R., & Radal, J. (2016). Rift-to-collision transition
1231 recorded by tectonothermal evolution of the northern Pyrenees : COOLING HISTORY OF
1232 THE NORTHERN PYRENEES. Tectonics, 35(4), 907-933.
1233 https://doi.org/10.1002/2015TC004016
1234 Valla, P. G., Herman, F., van der Beek, P. A., & Braun, J. (2010). Inversion of
1235 thermochronological age-elevation profiles to extract independent estimates of denudation
1236 and relief history — I : Theory and conceptual model. Earth and Planetary Science Letters,
1237 295(3-4), 511-522. https://doi.org/10.1016/j.epsl.2010.04.033
1238 Valla, P. G., van der Beek, P. A., & Braun, J. (2011). Rethinking low-temperature
1239 thermochronology data sampling strategies for quantification of denudation and relief
1240 histories : A case study in the French western Alps. Earth and Planetary Science Letters,
1241 307(3-4), 309-322. https://doi.org/10.1016/j.epsl.2011.05.003

1242 Valla, P. G., van der Beek, P. A., Shuster, D. L., Braun, J., Herman, F., Tassan-Got, L., &
1243 Gautheron, C. (2012). Late Neogene exhumation and relief development of the Aar and
1244 Aiguilles Rouges massifs (Swiss Alps) from low-temperature thermochronology modeling
1245 and ^{4}He/^{3}He thermochronometry. Journal of Geophysical Research: Earth Surface, 117(F1).
1246 https://doi.org/10.1029/2011JF002043
1247 van der Beek, P. A., Valla, P. G., Herman, F., Braun, J., Persano, C., Dobson, K. J., & Labrin, E.
1248 (2010). Inversion of thermochronological age–elevation profiles to extract independent
1249 estimates of denudation and relief history — II : Application to the French Western Alps.
1250 Earth and Planetary Science Letters, 296(1-2), 9-22.
1251 https://doi.org/10.1016/j.epsl.2010.04.032
1252 Vergés, J., Fernàndez, M., & Martìnez, A. (2002). The Pyrenean orogen : Pre-, syn-, and post-
1253 collisional evolution. Journal of the Virtual Explorer, 08.
1254 https://doi.org/10.3809/jvirtex.2002.00058
1255 Vergés, J., Millán, H., Roca, E., Muñoz, J. A., Marzo, M., Cirés, J., Bezemer, T. D., Zoetemeijer,
1256 R., & Cloetingh, S. (1995). Eastern Pyrenees and related foreland basins : Pre-, syn- and post-
1257 collisional crustal-scale cross-sections. Marine and Petroleum Geology, 12(8), 903-915.
1258 https://doi.org/10.1016/0264-8172(95)98854-X
1259 Vernant, P., Hivert, F., Chéry, J., Steer, P., Cattin, R., & Rigo, A. (2013). Erosion-induced
1260 isostatic rebound triggers extension in low convergent mountain ranges. Geology, 41(4),
1261 467-470. https://doi.org/10.1130/G33942.1
1262 Vernon, A. J., van der Beek, P. A., Sinclair, H. D., Persano, C., Foeken, J., & Stuart, F. M.
1263 (2009). Variable late Neogene exhumation of the central European Alps : Low-temperature
1264 thermochronology from the Aar Massif, Switzerland, and the Lepontine Dome, Italy:
1265 EXHUMATION OF THE CENTRAL EUROPEAN ALPS. Tectonics, 28(5).
1266 https://doi.org/10.1029/2008TC002387
1267 Waldner, M., Bellahsen, N., Mouthereau, F., Bernet, M., Pik, R., Rosenberg, C. L., & Balvay, M.
1268 (2021). Central Pyrenees Mountain Building : Constraints From New LT
1269 Thermochronological Data From the Axial Zone. Tectonics, 40(3).
1270 https://doi.org/10.1029/2020TC006614
1271 Wang, F., Feng, H., Shi, W., Zhang, W., Wu, L., Yang, L., Wang, Y., Zhang, Z., & Zhu, R.
1272 (2016). Relief history and denudation evolution of the northern Tibet margin : Constraints
1273 from 40Ar/39Ar and (U–Th)/He dating and implications for far-field effect of rising plateau.
1274 Tectonophysics, 675, 196-208. https://doi.org/10.1016/j.tecto.2016.03.001

Wessel, P., Luis, J. F., Uieda, L., Scharroo, R., Wobbe, F., Smith, W. H. F., & Tian, D. (2019). The Generic Mapping Tools Version 6. Geochemistry, Geophysics, Geosystems, 20(11), 5556-5564. https://doi.org/10.1029/2019GC008515

Whipple, K. X. (2009). The influence of climate on the tectonic evolution of mountain belts. Nature Geoscience, 2(2), 97-104. https://doi.org/10.1038/ngeo413

Whitchurch, A. L., Carter, A., Sinclair, H. D., Duller, R. A., Whittaker, A. C., & Allen, P. A. (2011). Sediment routing system evolution within a diachronously uplifting orogen : Insights from detrital zircon thermochronological analyses from the South-Central Pyrenees. American Journal of Science, 311(5), 442-482. https://doi.org/10.2475/05.2011.03

Willett, S. D. (1999). Orogeny and orography : The effects of erosion on the structure of mountain belts. Journal of Geophysical Research: Solid Earth, 104(B12), 28957-28981. https://doi.org/10.1029/1999JB900248

Zapata, S., Zapata-Henao, M., Cardona, A., Jaramillo, C., Silvestro, D., & Oboh-Ikuenobe, F. (2021). Long-term topographic growth and decay constrained by 3D thermo-kinematic modeling : Tectonic evolution of the Antioquia Altiplano, Northern Andes. Global and Planetary Change, 203, 103553. https://doi.org/10.1016/j.gloplacha.2021.103553

Zhang, Y.-Z., Replumaz, A., Wang, G.-C., Leloup, P. H., Gautheron, C., Bernet, M., van der Beek, P., Paquette, J. L., Wang, A., Zhang, K.-X., Chevalier, M.-L., & Li, H.-B. (2015). Timing and rate of exhumation along the Litang fault system, implication for fault reorganization in Southeast Tibet : LITANG FAULT SYSTEM EXHUMATION HISTORY. Tectonics, 34(6), 1219-1243. https://doi.org/10.1002/2014TC003671

Ziegler, P. A. (1992). European Cenozoic rift system. Tectonophysics, 208(1–3), 91–111. https://doi.org/10.1016/0040-1951(92)90338-7